Effects of Sea Spray on Large-Scale Climatic Features over the Southern Ocean

YAJUAN SONG,[a,b,c] FANGLI QIAO,[a,b,c] JIPING LIU,[d] QI SHU,[a,b,c] YING BAO,[a,b,c] MENG WEI,[a,b,c] AND ZHENYA SONG[a,b,c]

[a] *First Institute of Oceanography, Key Laboratory of Marine Science and Numerical Modeling, Ministry of Natural Resources, Qingdao, China*
[b] *Laboratory for Regional Oceanography and Numerical Modeling, Pilot National Laboratory for Marine Science and Technology, Qingdao, China*
[c] *Shandong Key Laboratory of Marine Science and Numerical Modeling, Qingdao, China*
[d] *Department of Atmospheric and Environmental Sciences, University at Albany, State University of New York, Albany, New York*

(Manuscript received 10 August 2021, in final form 9 February 2022)

ABSTRACT: The Southern Ocean, characterized by strong westerly winds and a rough sea state, exhibits the most pronounced sea spray effects. Sea spray ejected by ocean surface waves enhances heat and water exchange at the air–sea interface. However, this process has not been considered in current climate models, and the influence of sea spray on the coupled air–sea system remains largely unknown. This study incorporated a parameterization of the sea spray influence on latent and sensible heat fluxes into the First Institute of Oceanography Earth System Model version 2.0 (FIO-ESM v2.0), a climate model coupled with an ocean surface waves component. The results indicate that the spray-mediated enthalpy flux accounted for over 20%–50% of the total value. Sea spray promoted ocean evaporation and heat transport, resulting in air and ocean surface cooling and strengthened westerly winds. Furthermore, a moist and stable atmosphere favored an increase in cloud fraction over the Southern Ocean, particularly low-level clouds. Increased clouds reflected downward shortwave radiation and reduced solar radiation absorption at the surface. At present, the climate models participating in phase 6 of the Coupled Model Intercomparison Project (CMIP6) still suffer notable deficiencies in reasonably reproducing the climatological features of the Southern Ocean, including warm SST and underestimated clouds biases with more absorbed shortwave radiation. Our results suggest that consideration of sea spray effects is a feasible solution to mitigate these common biases and enhance the confidence in simulations and predictions with climate models.

KEYWORDS: Surface fluxes; Sea surface temperature; Cloud cover; Atmosphere-ocean interaction; Climate models; Southern Ocean

1. Introduction

Sea spray plays an important role in heat and water exchange at the air–sea interface (Ling and Kao 1976; Andreas 1992, 2003, 2005; Richter and Veron 2016; Peng and Richter 2019; Hartery et al. 2020; Sroka and Emanuel 2021). Large spray droplets ejected from the ocean effectively increase the ocean surface area (Andreas 2003). The droplets with the same temperature as that of the ocean surface directly transport sensible heat (SH) into the atmosphere. Water evaporates at the surface of these droplets, accomplished by the latent heat (LH) release process (Andreas 1992, 2003). Moreover, previous studies have pointed out that surface air must supply most heat to evaporate spray droplets, so these droplets constitute a SH sink (Fairall et al. 1994).

Under moderate and strong wind conditions, spray-mediated enthalpy flux accounts for a considerable proportion of the total heat flux, which cannot be ignored in the air–sea coupled system. Heat and water transfer at the air–sea interface follows two pathways, which are determined by the surface wind speed (Andreas et al. 2008, 2015). Under low wind conditions, heat and moisture exchange due to air–sea differences in humidity and temperature occurs almost exclusively at the air–sea interface. This interfacial pathway is controlled by molecular processes. Meanwhile, sea spray contributes to heat and moisture transfer with increasing wind speed, which is the spray flux pathway controlled by microphysical processes surrounding spray droplets (Andreas 1992, 2003). Previous studies have demonstrated that the spray-mediated flux becomes significant when the 10-m wind speed ranges from 10 to 15 m s^{-1} (Andreas and DeCosmo 2002). Further, the spray flux becomes comparable to the interfacial LH flux when the wind speeds up to 20 m s^{-1} (Fairall et al. 1994). Andreas et al. (2008) reported that sea spray contributes at least 10% to the total surface heat flux at fairly modest wind speeds (i.e., 11 m s^{-1} for the SH flux and 13 m s^{-1} for the LH flux). Moreover, Richter and Stern (2014) revealed that spray-mediated flux dominates the heat flux exchanges at the hurricane air–sea interface based on dropsonde data. Over the Southern Ocean, the wind speed generally ranges from 10 to 17 m s^{-1}, with instantaneous wind speed from shipboard ranging from 0.6 to 23.5 m s^{-1}, and even reaching up to 27.2 m s^{-1} based on Quick Scatterometer (QuikSCAT) satellite measurements (Ho et al. 2006). Therefore, sea spray effects should be reasonably considered.

Spray-mediated enthalpy fluxes have been estimated via different parameterization methods, which have been incorporated into various models, but this processes still represent

Denotes content that is immediately available upon publication as open access.

Corresponding authors: Zhenya Song, songroy@fio.org.cn; Jiping Liu, jliu26@albany.edu

DOI: 10.1175/JCLI-D-21-0608.1

a missing process in the climate model. Based on numerous observations and theory, a microphysical model of the above spray-mediated enthalpy fluxes has been proposed to calculate heat and water fluxes of spray droplets in the high-wind regime (Andreas 1992, 2003; Andreas et al. 1995). However, this microphysical model is too complex and computationally intensive to apply in a large-scale numerical model. Hence, Andreas et al. (2008) proposed a bulk spray-mediated flux algorithm, which allows quick simulation of the spray heat flux based on oceanic and atmospheric variables, without considering complete microphysical processes of sea spray. Previous studies have introduced the algorithm into a large-scale numerical model to reveal the effects of sea spray on the air–sea heat flux transfer process within tropical cyclones (Richter and Stern 2014; Zhao et al. 2017). In addition, this algorithm has been assessed via direct numerical simulations (Peng and Richter 2019). However, the abovementioned algorithm has never been applied in a climate model, and the climate system response to a small-scale sea spray event remains largely unknown.

The climate model is an important tool for simulating and predicting climate behavior on different time scales. However, it remains a long-standing challenge among climate models to correctly simulate the climatological state of Southern Ocean. Previous studies have examined the representation of cloud and radiation budgets based on climate model results during phases 3 and 5 of the Coupled Model Intercomparison Project (CMIP3 and CMIP5, respectively). The cloud fraction is generally underestimated in the climate model (Trenberth and Fasullo 2010; Soden and Vecchi 2011; Dolinar et al. 2015; Mason et al. 2015). The cloud liquid and ice water contents have not been reasonably simulated over the Southern Ocean (D'Alessandro et al. 2019). Consequently, less solar radiation is reflected, resulting in excess surface downward shortwave radiation (SWR) with a positive shortwave cloud radiation forcing (SCRF) bias up to 30 W m^{-2} (Trenberth and Fasullo 2010; Ceppi et al. 2012; Bodas-Salcedo et al. 2012; Li et al. 2013). Excessive solar radiation also leads to a pervasive warm sea surface temperature (SST) bias, and the magnitude of this bias is larger than 3°C (Wang et al. 2014). Certain studies have been performed to mitigate these common biases, for example, by improving the simulation of different cloud types or increasing the amount of supercooled liquid water in low-level clouds (Bodas-Salcedo et al. 2014, 2016; Kay et al. 2016). However, these pervasive biases entailing warm SST and underestimated cloud fraction still persist in state-of-the-art climate models (Kuma et al. 2020; Vignesh et al. 2020).

In this study, the bulk spray-mediated flux algorithm is incorporated into a climate model to explore the effects of sea spray on large-scale features of the Southern Ocean. The remainder of this paper is organized as follows: section 2 provides a description of the model, spray-mediated flux algorithm, observation datasets, and numerical experiments. Section 3 reveals the most profound effects of sea spray on the ocean and atmosphere and related physical processes. Finally, conclusions and a discussion are provided in section 4.

2. Model, experiments, and datasets

a. Model

The First Institute of Oceanography Earth System Model version 2.0 (FIO-ESM v2.0), which participated in phase 6 of the Coupled Model Intercomparison Project (CMIP6), was employed to evaluate sea spray effects. FIO-ESM v2.0 contains six model components (Bao et al. 2020): the Community Atmosphere Model version 5 (CAM5; Neale et al. 2010), the Parallel Ocean Program version 2 ocean model (POP2; Smith et al. 2010), the Community Land Model version 4 (CLM4; Lawrence et al. 2011), the Los Alamos National Laboratory sea ice model version 4 (CICE4; Hunke and Lipscomb 2008), the River Transport Model (Branstetter 2001), and the Marine Science and Numerical Modeling (MASNUM) wavenumber spectrum wave model (MASNUM-WAM) developed by the FIO (Qiao et al. 2016). CAM5 and CLM4 have a horizontal resolution of 1.25° longitude and 0.9° latitude. There are 30 vertical levels from the surface to the top of the atmosphere. In CAM5, the liquid and ice stratiform cloud fractions based on humidity are separately calculated (Gettelman et al. 2010). POP2, CICE4, and MASNUM-WAM exhibit a nonuniform horizontal resolution, approximately 1.1° in regard to the longitude and 0.27°–0.54° in regard to the latitude, with the North Pole displaced to Greenland. Model components are connected via Coupler 7, which is developed by the National Center for Atmospheric Research (Craig et al. 2011). The atmosphere, land surface, and sea ice component models exchange data with the coupler every 0.5 h, while the river runoff, ocean, and wave models exchange data with the coupler at 3-h intervals. The MASNUM-WAM obtains wind field at 10-m height of ocean surface and sea ice concentration from the coupler, is integrated to produce the wavenumber spectrum, then calculates the nonbreaking surface wave–induced vertical mixing and other necessary variables (e.g., significant wave height, denoted as Hs) for including sea spray on air–sea flux, and finally sends the nonbreaking surface wave–induced vertical mixing (Qiao et al. 2004) to POP2 at each ocean time step and other variables to the coupler every 3 h. Sea ice concentration is used to check whether the grid is covered by sea ice (sea ice concentration greater than 30%), where the wave spectrum is set to be zero. In this study, the MASNUM-WAM model provided real-time Hs data to calculate the LH and SH fluxes induced by sea spray. Moreover, global monthly mean and 3-h instantaneous wave parameter datasets based on the MASNUM-WAM model have been established and published (Song et al. 2020). The resultant climatological distributions Hs based on the output of MASNUM-WAM model and reanalysis datasets exhibit good agreement, which indicates that FIO-ESM v2.0 and MASNUM-WAM have the ability to simulate ocean surface waves.

FIO-ESM v2.0 was evaluated before the spray experiments were performed. Bao et al. (2020) evaluated the model simulation ability based on CMIP6 experiments results, including precipitation, SST, surface air temperature, Atlantic meridional overturning circulation, and El Niño–Southern Oscillation. Certain common simulation drifts occur in this model, for example, the double-intertropical convergence zone problem in the tropics and surface air temperature biases over

mountains and plateaus. However, the basic climate features are reasonably simulated, and the model biases are considerably smaller than those of the previous version, namely FIO-ESM v1.0 (Qiao et al. 2013; Bao et al. 2020).

To better understand the physical processes of sea spray effects on the coupled air–sea system in the Southern Ocean, two numerical experiments were designed and conducted: one experiment is a control run without sea spray effects, denoted as Exp_Ctrl, and the other experiment is a sensitivity experiment considering sea spray impacts, denoted as Exp_Spray. These two experiments were initialed from an equilibrium initial state anchored in preindustrial time (300 years, as shown in Fig. A1) and integrated over 165 years with all forcings prescribed from 1850 to 2014 (Eyring et al. 2016). Moreover, to reasonably compare observations and simulated clouds, the Cloud Feedback Model Intercomparison Project (CFMIP) Observation Simulator Package (COSP) was introduced in our model, and COSP-enabled simulations were provided. More information on the COSP can be found in Bodas-Salcedo et al. (2011).

b. Method

Andreas et al. (2015) proposed a bulk spray-mediated flux algorithm that facilitates quick calculations of the spray-mediated flux based on bulk oceanic and large-scale meteorological features. It is assumed that droplets with an initial radius 100 and 50 μm generate the most significant contribution to SH and LH fluxes. The LH ($H_{L,\mathrm{sp}}$) and SH ($H_{s,\mathrm{sp}}$) fluxes induced by sea spray are expressed as

$$H_{L,\mathrm{sp}} = \alpha\overline{Q_L} = \rho_w L_v \left\{1 - \left[\frac{r(\tau_{f,50})}{50\mu\mathrm{m}}\right]^3\right\} V_L(u_{*,B}), \tag{1}$$

$$H_{s,\mathrm{sp}} = \beta\overline{Q_S} - (\alpha - \gamma)\overline{Q_L} = \rho_w c_{\mathrm{ps}}(T_s - T_{\mathrm{eq},100}) V_S(u_{*,B}). \tag{2}$$

Throughout the integration process, the spray flux calculation depends on the current wind speed, air potential temperature, relative humidity (RH), Hs, SST, and sea surface salinity (SSS). All these variables, including the input and output of Eqs. (1) and (2) are introduced in appendix B.

In the above equations, α, β, and γ are nonnegative constants evaluated based on observations. Andreas and DeCosmo (1999) assumed that spray contributions to the latent ($\overline{Q_L}$) and sensible ($\overline{Q_S}$) heat fluxes should be added linearly to the interfacial fluxes. However, Fairall et al. (1994) pointed out that the droplet evaporation layer must supply most heat to evaporate spray droplets. Therefore, the droplets worked as the SH sink. As expressed in Eq. (1), the α term denotes the LH flux induced by droplet evaporation. The same term in Eq. (2) with the opposite sign indicates that SH is consumed by droplets for evaporation. The β term in Eq. (2) quantifies the SH transported by droplets as they transition from SST to the equilibrium temperature (Andreas 1992, 2003). In addition, under the effect of spray evaporation, the variable air–sea temperature difference contributes to SH transport, which is denoted as theγ term. The values of these constants remain inconclusive. Andreas (2003) assumed $\alpha = 3.3$, $\beta = 5.7$, and $\gamma = 2.8$. Andreas et al. (2008) determined that $\beta = 10.5$ is more appropriate. According to Andreas et al. (2015), it was assumed that measurements are more consistent with algorithm results for $\alpha = 2.46$, $\beta = 15.15$, and $\gamma = 1.77$.

Incorporation of this bulk spray–mediated flux algorithm into the climate model is a novel approach. Although this algorithm was proposed to calculate the flux under hurricanes conditions, it is also applicable over the Southern Ocean. First, the observations considered for parameterization not only include observations originating from the tropics but also include observations originating from mid and high-latitude regions, such as the Humidity Exchange over the Sea (HEXOS) experiment (DeCosmo et al. 1996, conducted over the North Sea), the Fronts and Atlantic Storm-Tracks Experiment (FASTEX; Persson et al. 2005), which is carried out along a transect across the North Atlantic), and the Greenland Flow Distortion experiment (Petersen and Renfrew 2009) performed over the Irminger Sea and Denmark Strait). Ocean surface waves are strong in these areas, and cyclone activities frequently occur under strong winds. The observed wind speed data employed for parameterization included values ranging from 5 to 25 m s^{-1}, which is similar to the wind speed range over the Southern Ocean. Second, in FIO-ESM v2.0, the Hs and wind fields with a 3-h temporal resolution could reflect the gustiness effects and extreme sea conditions that affect spray production. As shown in Fig. 1, the maximum wind speed even reached up to 30 m s^{-1}, with the annual mean wind speed generally ranging from 11 to 12 m s^{-1}. Meanwhile, the annual mean Hs value ranged from 4 to 5 m, and the maximum 3-h instantaneous Hs was higher than 18 m. Finally, the algorithm has been implemented globally. Liu et al. (2011) applied the spray-mediated flux algorithm on global scale to produce the satellite-derived flux product XSeaFlux. The comparison results suggested that the LH flux of the newly developed high-resolution XSeaFlux product is very similar to the considered observations.

The method of sea spray incorporated into the climate model is introduced. The heat fluxes, including both the interfacial and spray-mediated heat flux, are calculated in the coupler of FIO-ESM v2.0. Specifically, bulk equations control the interfacial heat flux based on the turbulent Monin–Obukhov similarity theory (Bryan et al. 1996). The spray-mediated heat flux is calculated based on variables of the ocean surface, atmospheric bottom layer, and wave model with different time intervals. The spray-mediated heat flux is added to the interfacial heat flux in the coupler and then fed to other model components. For example, in the atmosphere model, the effect of spray even influences high levels of the atmosphere. Due to the varying data exchange frequencies between each model component and the coupler, the 0.5-h mean air potential temperature and RH retrieved from the atmosphere model, 3-h SST and SSS from the ocean model, and 3-h Hs obtained from the wave model are applied in the fast spray-flux algorithm. In addition, the friction velocity $u_{*,B}$ is calculated in the coupler and updated with the wind field. All these terms, including $T_{\mathrm{eq},100}$, $r(\tau_{f,50})$, L_v, $V_S(u_{*,B})$, and $V_L(u_{*,B})$, are recalculated at each time step and each grid.

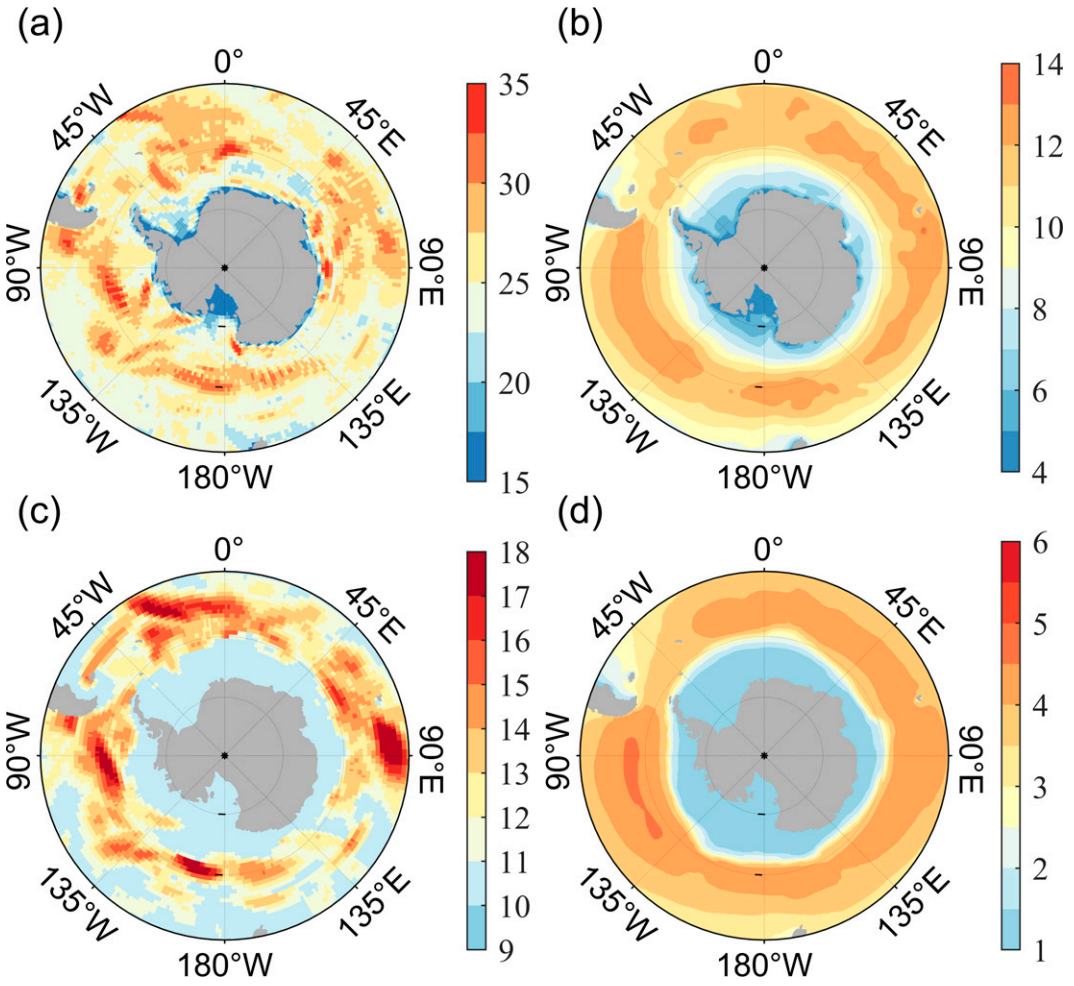

FIG. 1. 10-m wind speed and significant wave height simulated by FIO-ESM v2.0, (a) maximum 3-h instantaneous 10-m wind speed (unit: m s^{-1}), (b) annual mean 10-m wind speed (unit: m s^{-1}), (c) maximum 3-h instantaneous significant wave height (unit: m), and (d) annual mean significant wave height (unit: m).

c. *Data*

Several observation datasets were employed to evaluate the model performance, including the National Oceanic and Atmospheric Administration (NOAA) Optimum Interpolation Sea Surface Temperature v2 (OISST v2) product for the period from 1982 to 2014 with a horizontal resolution of 1° × 1° and the NOAA Extended Reconstructed Sea Surface Temperature version 5 (ERSST v5) product for the period from 1854 to 2014 in a 2° × 2° grid (Banzon et al. 2016; Huang et al. 2017). In addition, the simulated cloud fraction was compared to data retrieved from the Moderate Resolution Imaging Spectroradiometer (MODIS) dataset based on both *Aqua* and *Terra* satellite data for the period from 2003 to 2014 (Platnick et al. 2003).

According to CMIP6 design (Eyring et al. 2016), at least three realizations, named r1i1p1f1, r2i1p1f1, and r3i1p1f1 (the different ensemble members are distinguished by four ensemble axes: "r" denotes realization, "i" denotes initialization, "p" denotes physics, and "f" denotes forcing), should be provided for the historical simulation. The three realizations only differ in terms of initial conditions, which have almost no effect on the climatological analysis (Song et al. 2012). Therefore, the first realization (r1i1p1f1) of the monthly historical simulation from 35 CMIP6 climate models from 1982 to 2014 were compared to OISST v2 to assess the model performance in climatological SST simulation, including FIO-ESM v2.0. To our knowledge, FIO-ESM v2.0 is the only model that incorporates the influences of sea spray on the enthalpy flux in CMIP6. All information on relevant host centers and resolutions are summarized in Table 1. Before analysis, observational data and model outputs were linearly interpolated into a 1° × 1° grid.

3. Results

a. *Heat flux, humidity, and temperature*

The spray-mediated LH, SH, and net heat fluxes are shown in Fig. 2, represented by the differences between Exp_Spray and Exp_Ctrl. The stipples denote that the value is statistically

TABLE 1. Outputs of the CMIP6 climate models used in this study (more information and relevant references of each climate model can be found at https://esgf-node.llnl.gov/search/cmip6/).

No.	Model name	Institute	Country	Horizontal resolution of the ocean model
1	ACCESS-CM2	Commonwealth Scientific and Industrial Research Organisation	Australia	360 × 300
2	ACCESS-ESM1-5	Commonwealth Scientific and Industrial Research Organisation	Australia	360 × 300
3	BCC-CSM2-MR	Beijing Climate Center	China	360 × 232
4	BCC-ESM1	Beijing Climate Center	China	360 × 232
5	CanESM5	Canadian Centre for Climate Modelling and Analysis, Environment and Climate Change	Canada	360 × 291
6	CAS-ESM2-0	Chinese Academy of Sciences	China	360 × 196
7	CESM2	National Center for Atmospheric Research	United States	320 × 384
8	CESM2-FV2	National Center for Atmospheric Research	United States	320 × 384
9	CESM2-WACCM	National Center for Atmospheric Research	United States	320 × 384
10	CESM2-WACCM-FV2	National Center for Atmospheric Research	United States	320 × 384
11	CIESM	Department of Earth System Science, Tsinghua University	China	320 × 384
12	E3SM-1-0	Lawrence Livermore National Laboratory	United States	360 × 180
13	E3SM-1-1	Lawrence Livermore National Laboratory	United States	360 × 180
14	E3SM-1-1-ECA	Lawrence Livermore National Laboratory	United States	360 × 180
15	EC-Earth3	EC-Earth-Consortium	Sweden	362 × 292
16	EC-Earth3-Veg	EC-Earth-Consortium	Sweden	362 × 292
17	FGOALS-f3-L	Institute of Atmospheric Physics, Chinese Academy of Sciences	China	360 × 218
18	FGOALS-g3	Institute of Atmospheric Physics, Chinese Academy of Sciences	China	360 × 218
19	GFDL-CM4	Geophysical Fluid Dynamics Laboratory, National Oceanic and Atmospheric Administration	United States	360 × 180
20	GFDL-ESM4	Geophysical Fluid Dynamics Laboratory, National Oceanic and Atmospheric Administration	United States	360 × 180
21	GISS-E2-1-G	Goddard Institute for Space Studies, National Aeronautics and Space Administration	United States	144 × 90
22	GISS-E2-1-G-CC	Goddard Institute for Space Studies, National Aeronautics and Space Administration	United States	144 × 90
23	INM-CM4-8	Institute for Numerical Mathematics, Russian Academy of Science	Russia	360 × 180
24	INM-CM5-0	Institute for Numerical Mathematics, Russian Academy of Science	Russia	360 × 180
25	MCM-UA-1-0	Department of Geosciences, The University of Arizona	United States	192 × 80
26	MIROC6	Japan Agency for Marine-Earth Science and Technology	Japan	360 × 256
27	MPI-ESM-1-2-HAM	Max Planck Institute for Meteorology	Germany	256 × 220
28	MPI-ESM1-2-HR	Max Planck Institute for Meteorology	Germany	802 × 404
29	MPI-ESM1-2-LR	Max Planck Institute for Meteorology	Germany	256 × 220
30	MRI-ESM2-0	Meteorological Research Institute, Japan Meteorological Agency	Japan	360 × 363
31	NESM3	Nanjing University of Information Science and Technology	China	362 × 292
32	NorCPM1	Center for International Climate and Environmental Research, Norwegian Meteorological Institute, Nansen Environmental and Remote Sensing Center, Norwegian Institute for Air Research, University of Bergen, University of Oslo, and Uni Research	Norway	320 × 384
33	NorESM2-LM	Center for International Climate and Environmental Research, Norwegian Meteorological Institute, Nansen Environmental and Remote Sensing Center, Norwegian Institute for Air Research, University of Bergen, University of Oslo, and Uni Research	Norway	360 × 385
34	NorESM2-MM	Center for International Climate and Environmental Research, Norwegian Meteorological Institute, Nansen Environmental and Remote Sensing Center, Norwegian Institute for Air Research, University of Bergen, University of Oslo, and Uni Research	Norway	360 × 385

significant at the 95% confidence level. In this study, the downward (upward) direction was considered as positive (negative), indicating that the ocean absorbs (emits) heat. In the midlatitude region (from 30° to 45°S), less LH is lost from the ocean. However, in the high-latitude region (from 45° to 60°S), spray droplets are evaporated accompanied by enhanced LH release. In addition, more SH is transported to the atmosphere due to the spray effects, with a negative difference in most areas of the Southern Ocean, particularly at approximately 60°S. The area-averaged changes in LH and SH flux reached −2.23 and −0.67 W m^{-2}, respectively, within the latitude band bounded by 40° and 65°S. In addition, positive SH and LH flux anomalies were found along the Antarctic continent. Combining the obtained changes in both LH

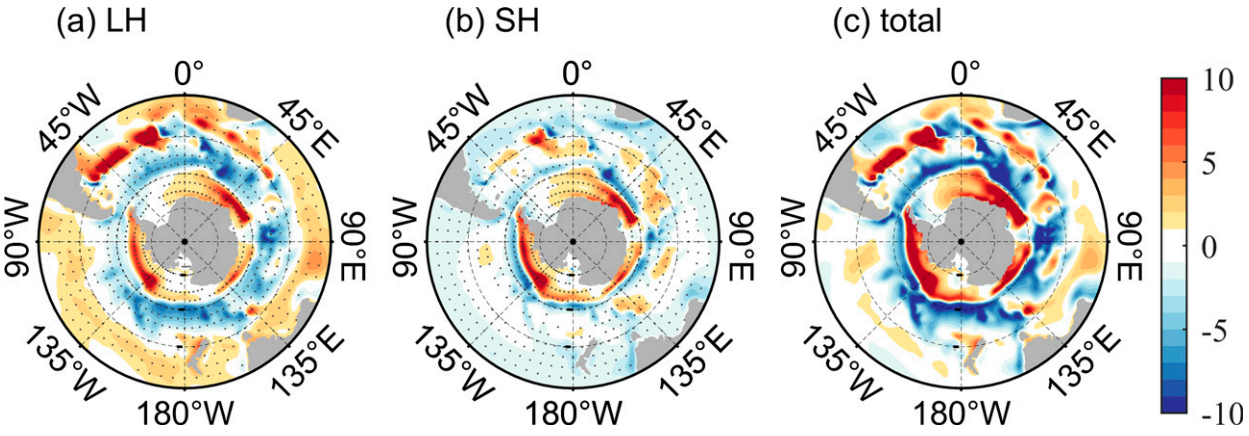

FIG. 2. Spray-mediated heat flux (unit: W m^{-2}), indicated by the differences between Exp_Spray and Exp_Ctrl: (a) latent heat (LH) flux, (b) sensible heat (SH) flux, and (c) total heat flux (the sum of the LH and SH heat fluxes). A positive value (downward flux) indicates that the ocean absorbs heat. The interval of latitude lines is 15°. A two-sample *t* test is applied, and the stippling denotes the values that are statistically significant at the 95% confidence level.

and SH, the difference in the net heat flux exhibited a large negative value in the mid- to high-latitude regions of the Southern Ocean, with the difference in the net heat flux less than -10 W m^{-2} at approximately 60°S.

To examine the effect of sea spray in the whole atmosphere, a vertical profile of the air temperature and the RH differences between Exp_Spray and Exp_Ctrl are shown in Fig. 3. All variables are meridionally averaged between 45° and 60°S. There are positive RH anomalies in the lower troposphere, especially below 700 hPa, while negative anomalies were distributed above 300 hPa. This suggests that the lower troposphere becomes wetter and the higher troposphere becomes dryer due to sea spray effects. Moreover, because of enhanced evaporation cooling effects on the atmosphere, the air temperature at lower levels decreased by approximately 1°C, which is consistent with the observed result of temperature variation (Andreas et al. 1995).

The lower atmosphere becomes moister and more stable due to sea spray. Droplets suspended in air influence the moisture distribution. Figure 4a shows the difference in RH at 2 m between Exp_Spray and Exp_Ctrl. RH increases in the lower atmosphere from 45°S to high latitudes. Furthermore, the changes in heat and moisture caused by sea spray alter the stability of the atmosphere. Here, the potential pseudoequivalent temperature (PPET) difference between 700 and 1000 hPa was analyzed to reveal the change in atmospheric stability in the lower atmosphere. The PPET difference between these two experiments was positive over the entire Southern Ocean (Fig. 4b), indicating that a more stable low-level atmosphere formed under the effects of sea spray.

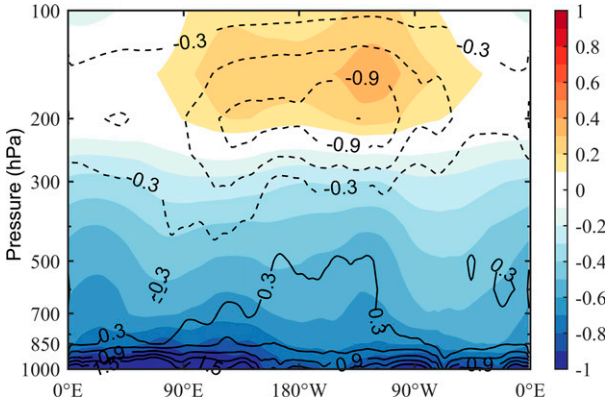

FIG. 3. Vertical profile of the meridional mean (45°–60°S) air temperature (shading; unit: °C) and relative humidity (contours; unit: %) differences between Exp_Spray and Exp_Ctrl.

Previous studies have demonstrated that reasonable SST simulation over the Southern Ocean remains a challenge for climate models (Wang et al. 2014). We evaluated the ability of 35 climate models in CMIP6 to simulate SST (Fig. 5), and the multimodel mean bias is shown in the last panel. Most climate models (23 out of 35) have warm SST biases compared with the OISST v2 dataset. The multimodel mean result also exhibited a warm bias, which was more obvious in the Atlantic and Indian sections of the Southern Ocean, with biases up to 2°–3°C. In contrast, several models could simulate SST well, for example, CanESM5 and GFDL-CM4, with small biases over the Southern Ocean. Held et al. (2019) indicated that excessive absorbed SWR biases were improved in GFDL-CM4 simulation. This suggests that less radiation absorption probably contributes to small SST biases.

The effect of sea spray profoundly influences SST. Figure 6 shows the annual mean SST in Exp_Ctrl and Exp_Spray compared to the OISST v2 dataset. Similar to the CMIP6 multimodel mean results, large warm SST bias was distributed in Exp_Ctrl, especially in the Indian Ocean and Atlantic Ocean sectors. The area-averaged (45°–60°S, 0°–360°E) SST difference between Exp_Ctrl and OISST v2 reached 1.68°C (Fig. 6a). By incorporating sea spray effects, the SST decreased due to evaporative cooling, with a maximum reduction of 2.73°C (Fig. 6c). As indicated in Fig. 6b, although the simulated SST was still higher than those in the OISST v2 dataset, this bias

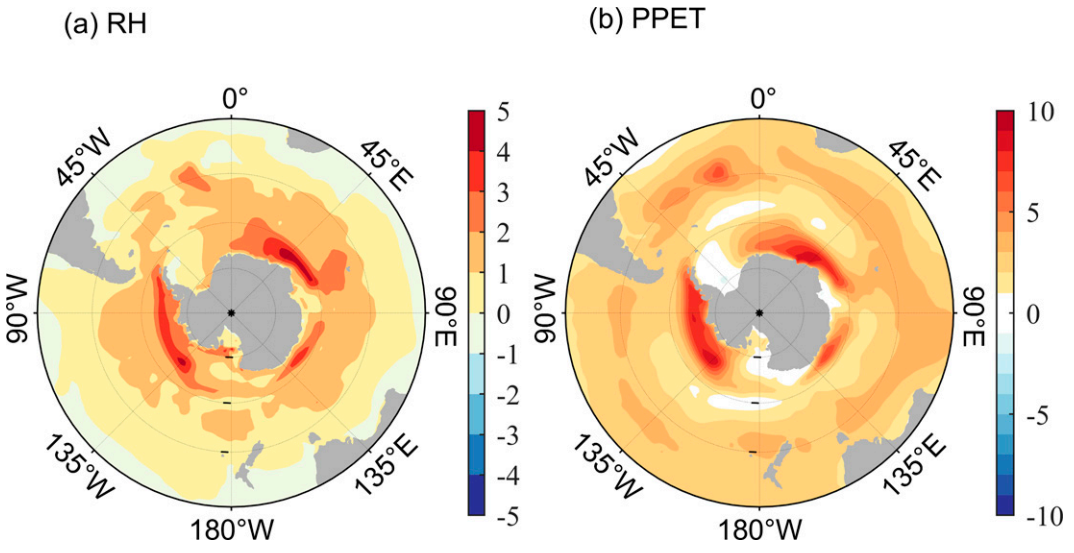

FIG. 4. (a) Differences in the climatological relative humidity at 2 m (unit: %) between Exp_Spray and Exp_Ctrl. (b) Differences in the atmospheric stability represented by the vertical variation in the potential pseudoequivalent temperature (700 hPa minus 1000 hPa; unit: 10^{-3} K hPa^{-1}) between Exp_Spray and Exp_Ctrl.

decreased from 1.68° to 0.97°C. Therefore, consideration of the sea spray effects could mitigate 42% of the warm SST bias over the Southern Ocean.

Both the air temperature and SST decreased under the influence of sea spray, leading to a smaller air–sea temperature difference. Figure 7 shows the differences between the air potential temperature at 1000 hPa and SST (a negative value indicates that SST is higher than the air potential temperature, and vice versa). Before considering the effect of sea spray, in Exp_Ctrl, the ocean was warmer than the atmosphere over most of the Southern Ocean (Fig. 7a). Then, both SST and air potential temperature decreased, but SST cooling was more obvious than the change in air potential temperature. These inconsistent variations in the temperature contributed to a reduction in air–sea temperature differences. In addition, the interfacial SH flux was determined considering

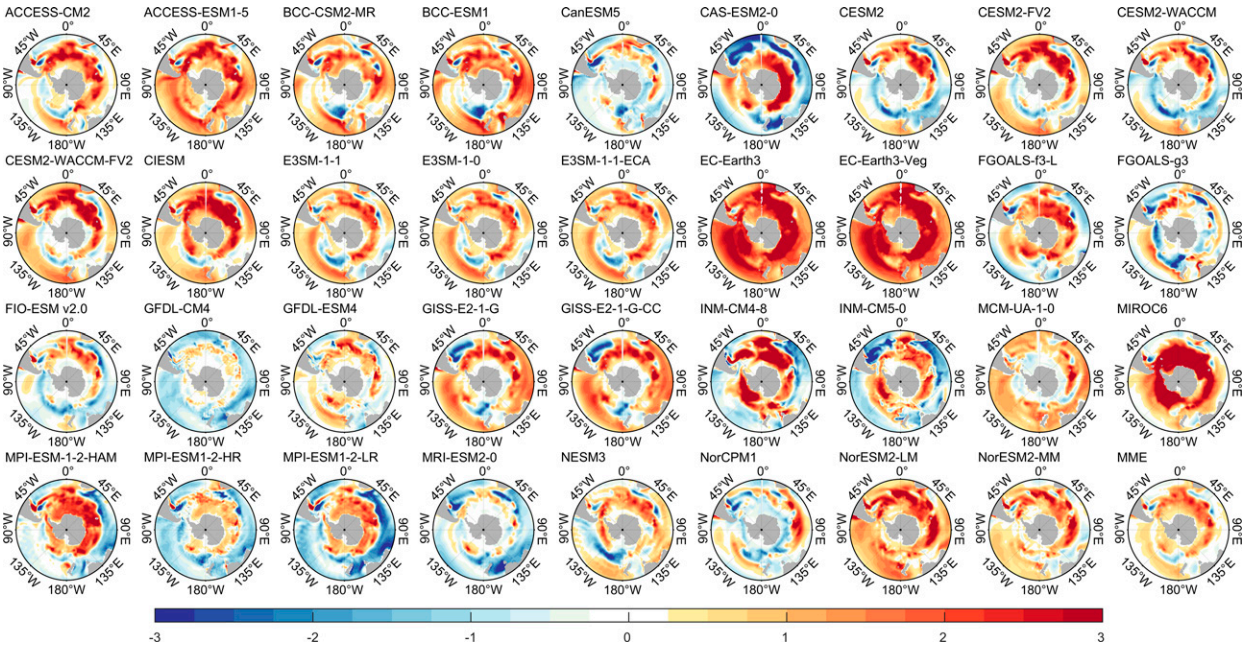

FIG. 5. Climatological SST based on historical runs of 35 CMIP6 models compared to OISSTv2.0 from 1982 to 2014 (unit: °C). MME in the bottom right corner shows the multimodel mean bias.

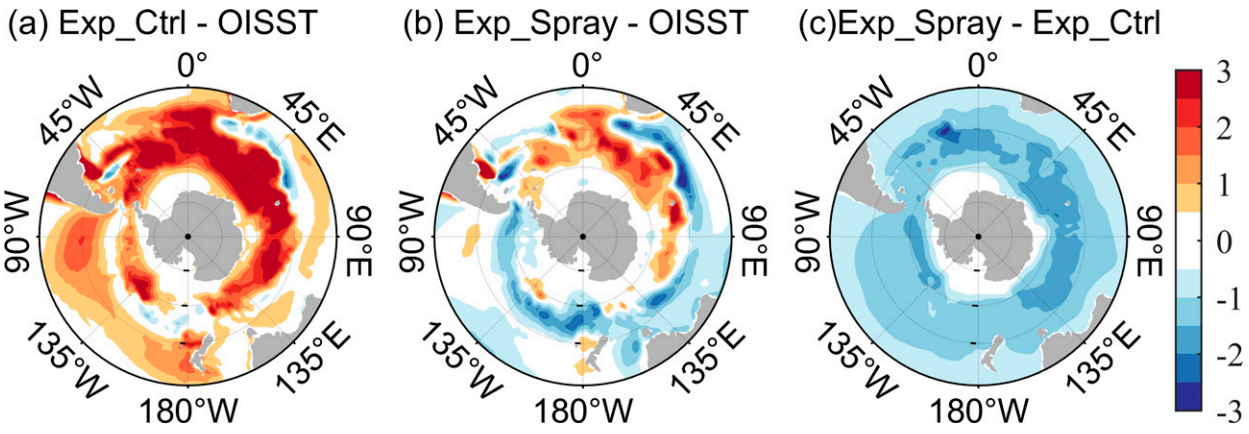

FIG. 6. Climatological sea surface temperature (SST) differences (unit: °C) from 1982 to 2014 between (a) Exp_Ctrl and OISST v2.0, (b) Exp_Spray and OISST v2.0, and (c) Exp_Spray and Exp_Ctrl.

the above air–sea temperature and humidity differences. As such, a smaller air–sea temperature difference prevented the interfacial SH flux from being released from the ocean.

The sea ice fraction increased due to the decrease in the air potential temperature and SST. As shown in Fig. 7c, the sea ice fraction increases by 5%–25% over the ocean close to the Antarctic continent (south of 60°S). Sea ice inhibits heat and moisture transport from the ocean into the atmosphere. Thus, LH and SH exchange was inhibited, featuring by a pronounced positive anomaly along the Antarctic continent (Figs. 2a and 2b, respectively).

b. *Cloud and radiation fluxes*

Sea spray profoundly impacts cloud formation, further influencing the surface radiation flux over the Southern Ocean. Figure 8 shows the differences in the cloud fraction, surface radiation flux, and cloud radiation forcing between Exp_Spray and Exp_Ctrl. Here, low-, middle-, and high-level clouds are bounded by the pressure levels of 700, 700–400, and 400 hPa to the top of the model, respectively. The low-level cloud fraction increased, with a maximum value of approximately 6% in the Indian Ocean sector. The changes in middle- and high-level clouds were not as notable as those in low-level clouds. As shown in Fig. 8c, the total cloud fraction increased, exhibiting a similar spatial pattern to that of the low-level cloud fraction. Clouds are strongly linked to RH and atmospheric stability in the marine boundary layer. The largest increase in RH below 700 hPa (Fig. 3) favored more low-level clouds. Moreover, more stable conditions in the lower troposphere, as revealed by the PPET difference between 700 and 1000 hPa (Fig. 4b), provided favorable conditions for low-level cloud formation. Increased cloud fraction reflects more incoming solar radiation away from the sea surface. As a result, less SWR is absorbed by the ocean, whereas

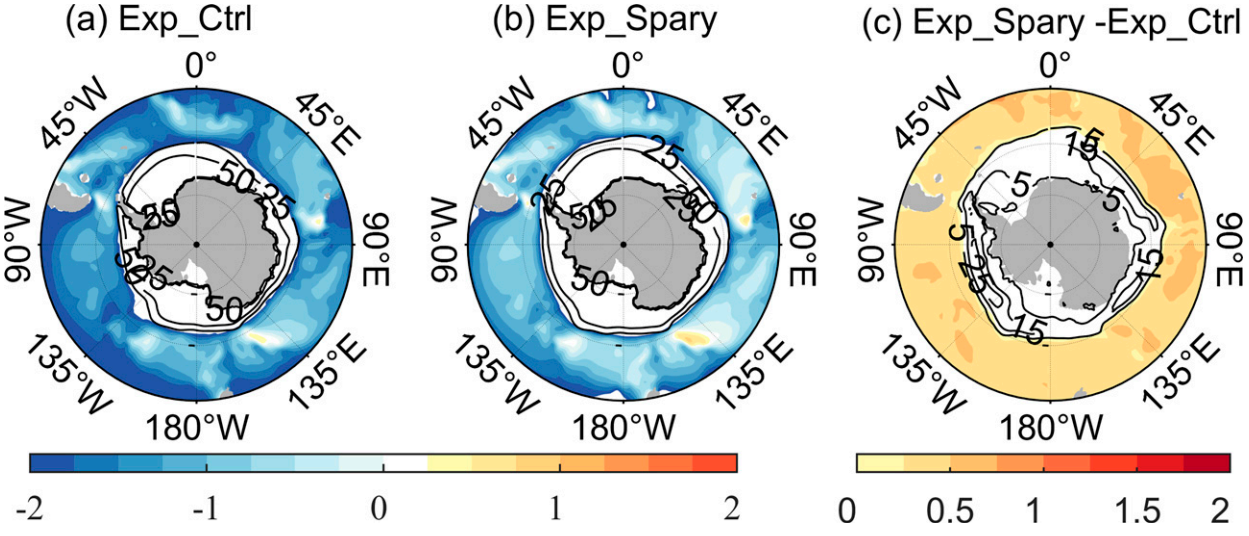

FIG. 7. Air–sea temperature difference between the air temperature at 1000 hPa and the sea surface temperature (SST; shading; unit: °C); the contours indicate the sea ice fraction (unit: %) in (a) Exp_Ctrl, (b) Exp_Spray, and (c) Exp_Spray − Exp_Ctrl. Air–sea temperature differences smaller than −2°C in (a) and (b) or covered by sea ice in (c) are not shown.

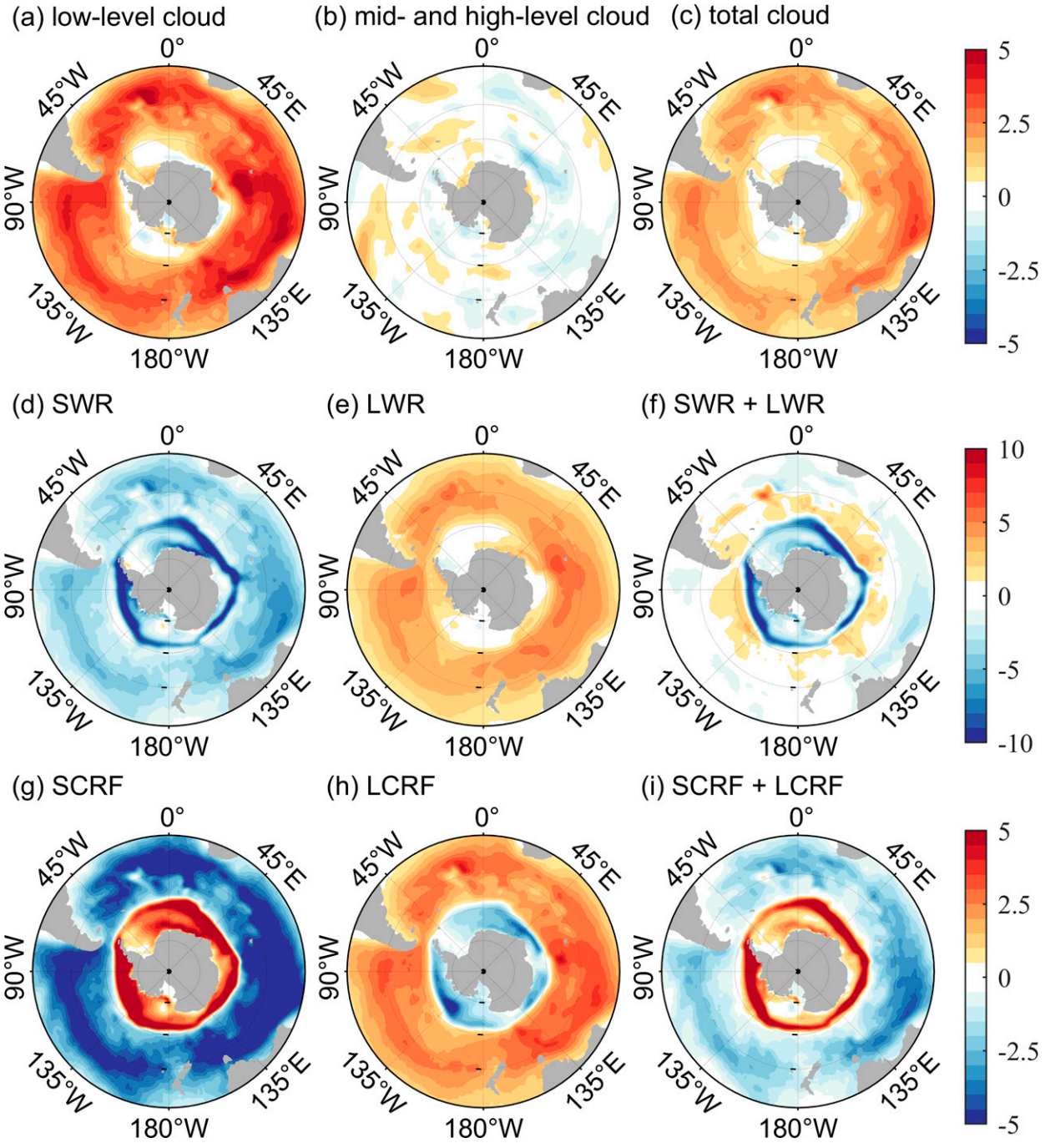

FIG. 8. Changes in the cloud fraction (unit: %) at the different levels, surface radiation flux (unit: W m^{-2}), and cloud radiation forcing (unit: W m^{-2}) due to sea spray, represented by the differences between Exp_Spray and Exp_Ctrl: (a) low-level cloud fraction, (b) mid- and high-level cloud fractions, (c) total cloud fraction, (d) shortwave radiation (SWR) at the surface, (e) longwave radiation (LWR) at the surface, (f) net radiation flux (including SWR and LWR), (g) shortwave cloud radiation forcing (SCRF), (h) longwave cloud radiation forcing (LCRF), and (i) net cloud radiation forcing.

the downward longwave radiation (LWR) is enhanced due to the increased cloud fraction. Figures 8d–f show differences in the surface SWR, LWR, and net radiation flux between Exp_Spray and Exp_Ctrl. Here, the downward radiation flux that is positive (negative) indicates that the ocean absorbs more (less) radiation. By incorporating sea spray effects, less SWR was absorbed due to more clouds. This suggested that the radiation bias attributed to excessive incoming SWR heat

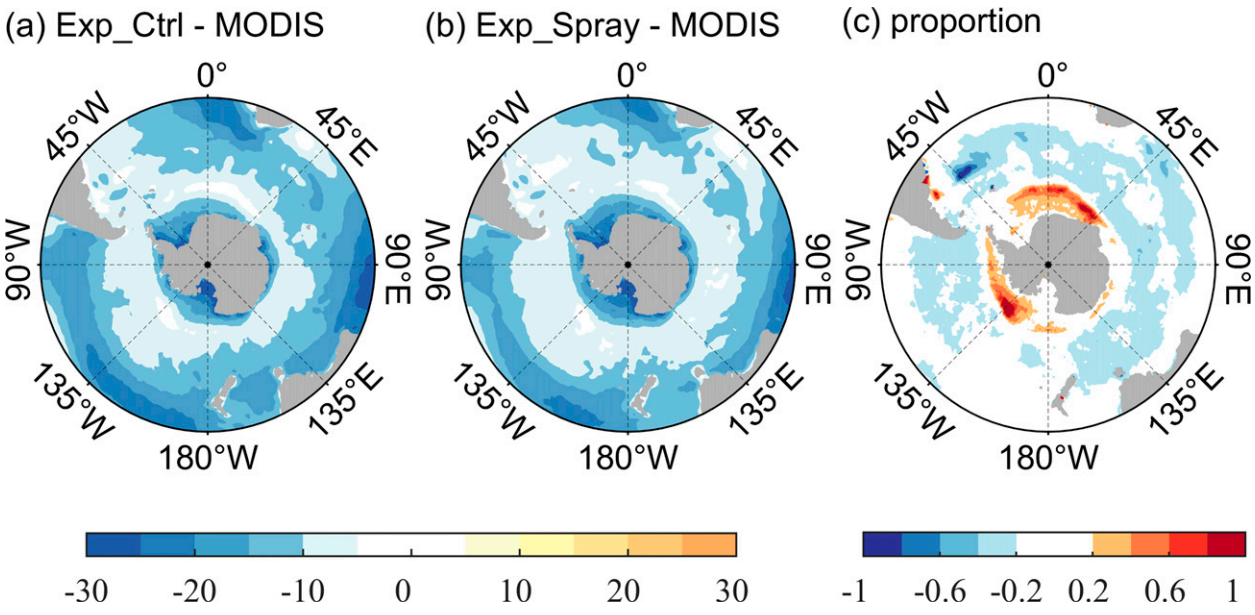

FIG. 9. COSP-enabled simulation of the climatological total cloud fraction compared to the MODIS climatology (based on both *Aqua* and *Terra* satellite data; unit: %) from 2003 to 2014: (a) Exp_Ctrl − MODIS and (b) Exp_Spray − MODIS. (c) The proportion of the variations due to sea spray (differences between Exp_Spray and Exp_Ctrl) to the simulated bias between the Exp_Ctrl and MODIS results.

absorption could be alleviated by considering spray. Moreover, increased clouds prevented the outgoing LWR flux, leading to enhanced downward LWR (Fig. 8e). Less SWR and more LWR with opposite directions were offset at the surface. In addition, the change in sea ice impeded radiation flux transport. The negative difference near the Antarctic continent, as shown in Figs. 8d and 8f, indicates that the ocean absorbed less SWR due to sea ice.

We further analyzed the changes in cloud radiative forcing due to sea spray. Clouds exert two competing effects on the radiation budget: surface cooling through SWR blocking and surface warming by preventing the outgoing LWR. Two effects were examined based on the surface cloud radiative forcing. As shown in Fig. 8g, the surface SCRF was negative because of less SWR absorption. In addition, the corresponding longwave cloud radiation forcing (LCRF) was positive, representing an increase in downward LWR under the sea spray effects (Fig. 8h). Thus, the above two radiative forcings counteracted each other locally, leading to a net cloud radiative forcing with a cooling effect over the Southern Ocean.

Incorporation of sea spray into FIO-ESM v2.0 could reduce the simulation bias of cloud cover. Currently, state-of-the-art climate models still experience difficulties in reasonably simulating climatological cloud cover characteristics. As mentioned above, the underestimated cloud fraction accompanied by an excessive incoming SWR over the Southern Ocean represents a common problem in climate models (Trenberth and Fasullo 2010). Inclusion of the sea spray effects could alleviate the underestimated cloud bias. In this study, to evaluate the model performance in cloud simulation, the COSP was incorporated into FIO-ESM v2.0 to include the COSP output (Bodas-Salcedo et al. 2011). Certain configurations of COSP in CAM5 followed those reported in Kay et al. (2012), and the MODIS climatology was employed to evaluate the model results. The total cloud fraction was grossly underestimated in both Exp_Ctrl and Exp_Spray (Fig. 9). However, more clouds were formed in the moister atmosphere by considering the sea spray effects. Figure 9c shows the proportion of the increased total cloud fraction due to sea spray (the differences between Exp_Spray and Exp_Ctrl) to the bias between the Exp_Ctrl and MODIS results. The proportion ranged from approximately −20% to −40% over the Southern Ocean. Here, we revealed that the bottom boundary process related to air–sea interaction could influence the simulation of clouds. Moreover, the development of cloud physical parameterization based on more observations, understanding cloud–climate feedback mechanisms, and credible representations of cloud processes in climate models remain important for cloud simulation improvement.

Analysis of the changes in cloud properties was performed to reveal the influence of sea spray on clouds. Cloud water paths were classified as cloud liquid water path (CLWP) or cloud ice water path (CIWP), representing the cloud liquid water and ice contents, respectively. The effect of sea spray on CLWP and CIWP is shown in Fig. 10. The CLWP increased from 30° to 60°S, exhibiting a peak at approximately 45°S, while an increased CIWP was distributed over the Southern Ocean with a distinct maximum at high latitudes. The change in the CLWP was much larger than that in the CIWP. Sea spray impacted both the liquid and ice cloud amounts. We further analyzed vertical profiles of liquid and ice cloud amounts meridional averaged from 45° to 60°S (Fig. 11). The liquid cloud amount increased in the lower atmospheric boundary layer (from the surface to 850 hPa)

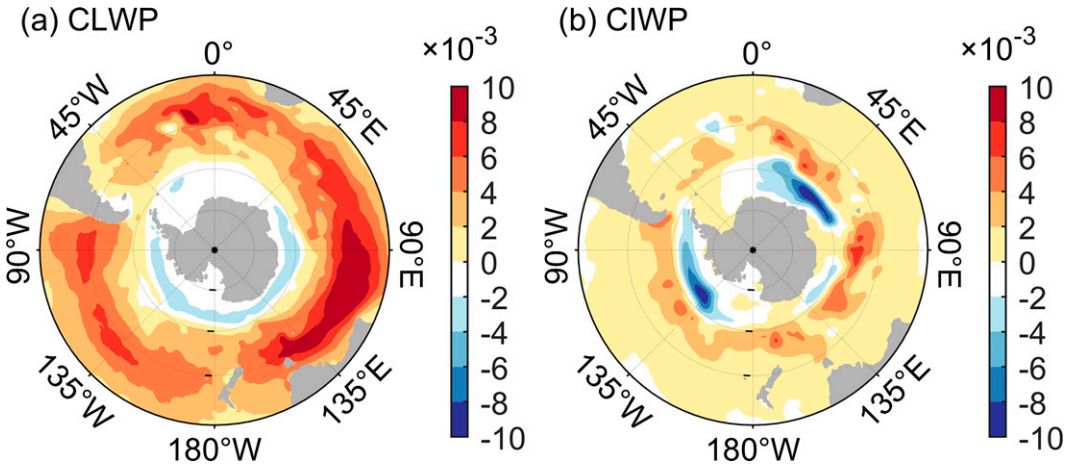

FIG. 10. Differences in the (a) cloud liquid water path and (b) cloud ice water path between Exp_Spray and Exp_Ctrl (unit: 10^{-3} kg m^{-2}).

and slightly decreased in the atmosphere from 850 to 500 hPa. This increase in the liquid cloud amount was pronounced near the sea surface. In addition, the ice cloud amount increased from 850 to 500 hPa and decreased in the upper atmosphere. This result demonstrated that the liquid cloud amount increased in the atmospheric boundary layer (below 850 hPa) and the ice cloud amount mainly increased above this layer from 850 to 500 hPa. Previous studies have indicated that an increased in supercooled cloud liquid by modifying the shallow convection scheme substantially reduces excessive absorbed SWR biases (Kay et al. 2016; Lasher-Trapp et al. 2021). In this work, the effects of sea spray contributed to increased liquid cloud amounts, which also provided favorable conditions to increase the cloud cover and reduce the incident radiation over the Southern Ocean.

c. Wind and sea level pressure

Sea spray not only influences the thermodynamic process in the air–sea coupled system but also affects the atmospheric circulation by modulating heat and moisture transport. Figure 12 shows the differences in the wind field at 1000 hPa and the sea level pressure (SLP) between Exp_Spray and Exp_Ctrl. An anomalously low SLP was distributed in the mid- and high-latitude regions of the Southern Ocean, accompanied by an anomalously high SLP to the north. As a result, the pressure gradient increased, which favored a stronger Antarctic Oscillation. The wind speed was enhanced with a maximum value of up to 1.0 m s^{-1} in the midlatitude region of the Southern Ocean. However, the midlatitude westerly winds simulated in Exp_Ctrl were notably stronger than those in the reanalysis datasets. Consideration of sea spray processes did not improve the wind simulation performance (not shown).

d. Direct and indirect effects

The zonal mean relevant variable differences are shown in Fig. 13 to quantify the influence of sea spray on the atmosphere

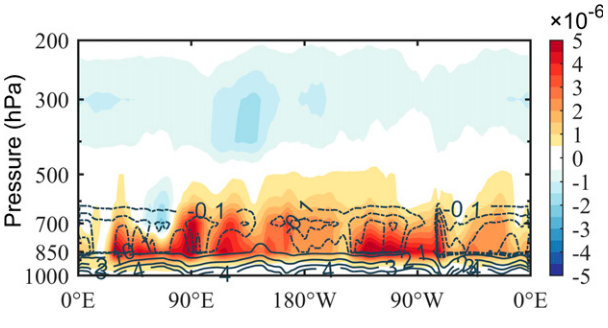

FIG. 11. Longitude–height vertical profiles of the meridional mean (45°–60°S) ice cloud amount (shading; unit: 10^{-6} kg kg^{-1}) and liquid cloud amount (contours; unit: 10^{-6} kg kg^{-1}) variations due to sea spray. The interval of the dashed contours is 0.1×10^{-6}, and the interval of the solid contours is 1×10^{-6}.

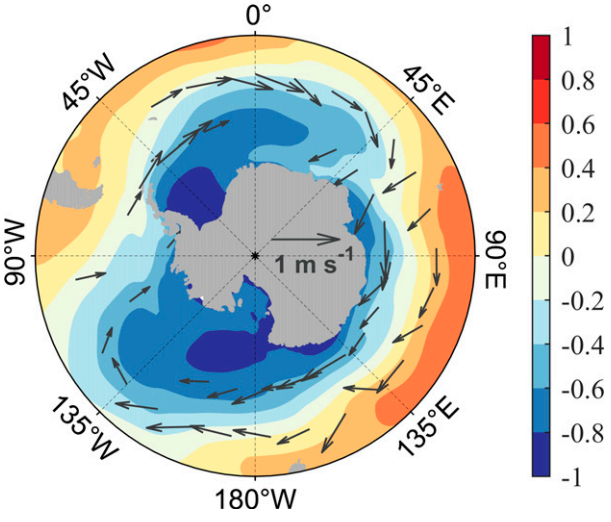

FIG. 12. Differences in the climatology sea level pressure (shading; unit: hPa) and wind field at 1000 hPa (vectors; unit: m s^{-1}) between Exp_Spray and Exp_Ctrl. Winds with speeds higher than 0.2 m s^{-1} are plotted.

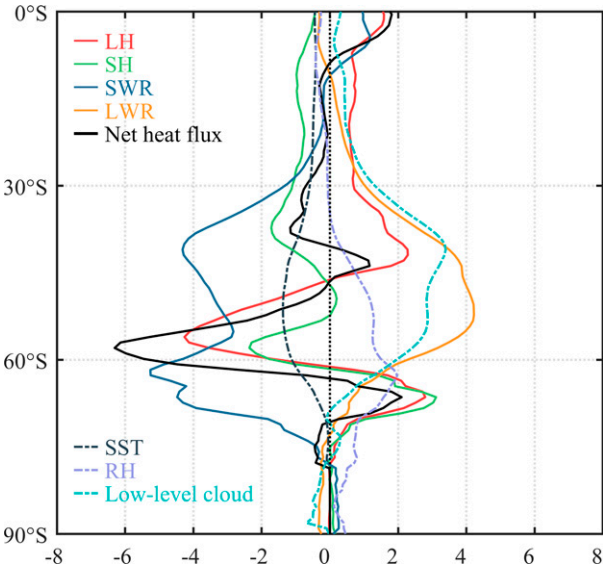

FIG. 13. Zonal mean differences between Exp_Spray and Exp_Ctrl in the latent heat flux (LH; solid red line; unit: W m^{-2}), sensible heat flux (SH; solid green line; unit: W m^{-2}), surface net shortwave radiation (SWR; solid blue line; unit: W m^{-2}), surface net longwave radiation (LWR; orange solid line; unit: W m^{-2}), net heat flux (black solid line, unit: W m^{-2}), sea surface temperature (SST; black dashed line; unit: °C), relative humidity (RH) at 2 m (purple dashed line; unit: %), and low-level cloud fraction (cyan dashed line; unit: %).

and ocean, with the positive (negative) value toward downward (upward) direction. The upward LH anomalies were mainly distributed from 45° to 60°S with a minimum value lower than -4 W m^{-2}. The SH anomalies were negative in most of the Southern Hemisphere, featuring a minimum value lower than -2 W m^{-2}. Both heat flux changes resulted in a notable heat loss (greater than 6 W m^{-2}) from 45° to 60°S. Moreover, more evaporation and heat transport tended to increase the air humidity. The zonally averaged RH value increases from 40° to 70°S. Under the effects of sea spray on RH, the low-level cloud fraction increased from 30° to 60°S with a maximum of up to 3%. As a result, the ocean surface absorbed less SWR (lower than -4 W m^{-2}), and an increased cloud cover also contributed to the downward LWR. The negative SWR was nearly entirely compensated by an enhanced incoming LWR (greater than 4 W m^{-2}). In general, the evaporative cooling effect caused by LH contributed to a decrease in SST reduction, with a zonal mean difference smaller than -1.5°C over the Southern Ocean.

We attempted to estimate the indirect and direct effects of sea spray on the heat flux, even though there exists an interaction between these effects. As defined in Eqs. (1) and (2), the sea spray–induced heat fluxes retrieved from Andreas et al. (2015) represent the direct sea spray effects. This effect is governed by sea spray droplets associated with microphysical processes at the droplets' surfaces. In addition, the ambient condition changing due to sea spray notably influences interfacial heat transport. First, the air temperature, SST, and humidity changed due to sea spray. As a result, air–sea temperature and humidity differences altered the interfacial heat transport process. Second, we found that westerly winds increased because of air temperature and surface air pressure gradients changes. Stronger winds could enhance interfacial heat transport. Finally, there occurred specific complex processes related to clouds in a fully coupled system. Spray droplets increased the air humidity, and more clouds were distributed over the Southern Ocean. By blocking excessive solar radiation absorption, SST decreased, which in turn influenced interfacial heat transport. We regard these variations as the indirect sea spray effects, calculated by the total heat flux in Exp_Spray minus the direct effect of sea spray and interfacial heat fluxes in Exp_Ctrl.

The direct and indirect effects of sea spray on the LH and SH fluxes are shown in Fig. 14. Both the LH and SH anomalies under the direct sea spray effects are negative (Figs. 14a and 14b, respectively). More LH and SH were released from the Southern Ocean, with the maximum difference in the LH flux up to -29.5 W m^{-2} located in the Indian sector. In contrast, the indirect sea spray effects on the LH and SH fluxes were positive from 30° to 60°S. These positive heat flux anomalies (preventing heat loss from the ocean) due to the indirect sea spray effects counteracted the negative changes (promoting heat loss from the ocean) attributed to the direct effects. Figures 14e and 14f show the proportion of the heat flux variations due to direct effect relative to the total changes of heat flux. The proportions of LH resulting from sea spray ranged from 20% to 40%. In regard to SH, the proportions even exceeded 50% over the Southern Ocean.

The effects of sea spray on large-scale features over the Southern Ocean were summarized in a schematic diagram (Fig. 15). All the variables were averaged over the latitude band extending from 45° to 60°S. The LH and SH fluxes caused by the direct effects of sea spray were negative, with values of -15.57 and -6.41 W m^{-2}, respectively. SST decreased by 1.3°C due to the spray-mediated flux. The SST reduction limited surface evaporation. As a result, the change in the interfacial LH flux was positive and to counteracted the negative LH flux caused by the direct spray effect. In addition, the positive air–sea temperature differences limited interfacial SH transport, which also exhibited the opposite sign with SH impacted by the direct spray effect. Moreover, incorporation of sea spray into FIO-ESM v2.0 also influenced clouds and radiation flux. An increased humidity and stability in the lower atmosphere led to an increased cloud fraction, particularly the low-level clouds (2.76%). As a result, less downward SWR was absorbed, with an anomalous SCRF value of -2.81 W m^{-2}. Meanwhile, the increased cloud fraction resulted in an enhanced downward LWR at the surface, with an anomalous LCRF value of 2.14 W m^{-2}. In general, the net cloud radiation forcing was negative over the Southern Ocean, revealing that the ocean absorbed less of the radiation flux.

4. Conclusions and discussion

Sea spray exerts nonnegligible effects on air–sea heat and water exchange. The spray-mediated enthalpy flux calculated

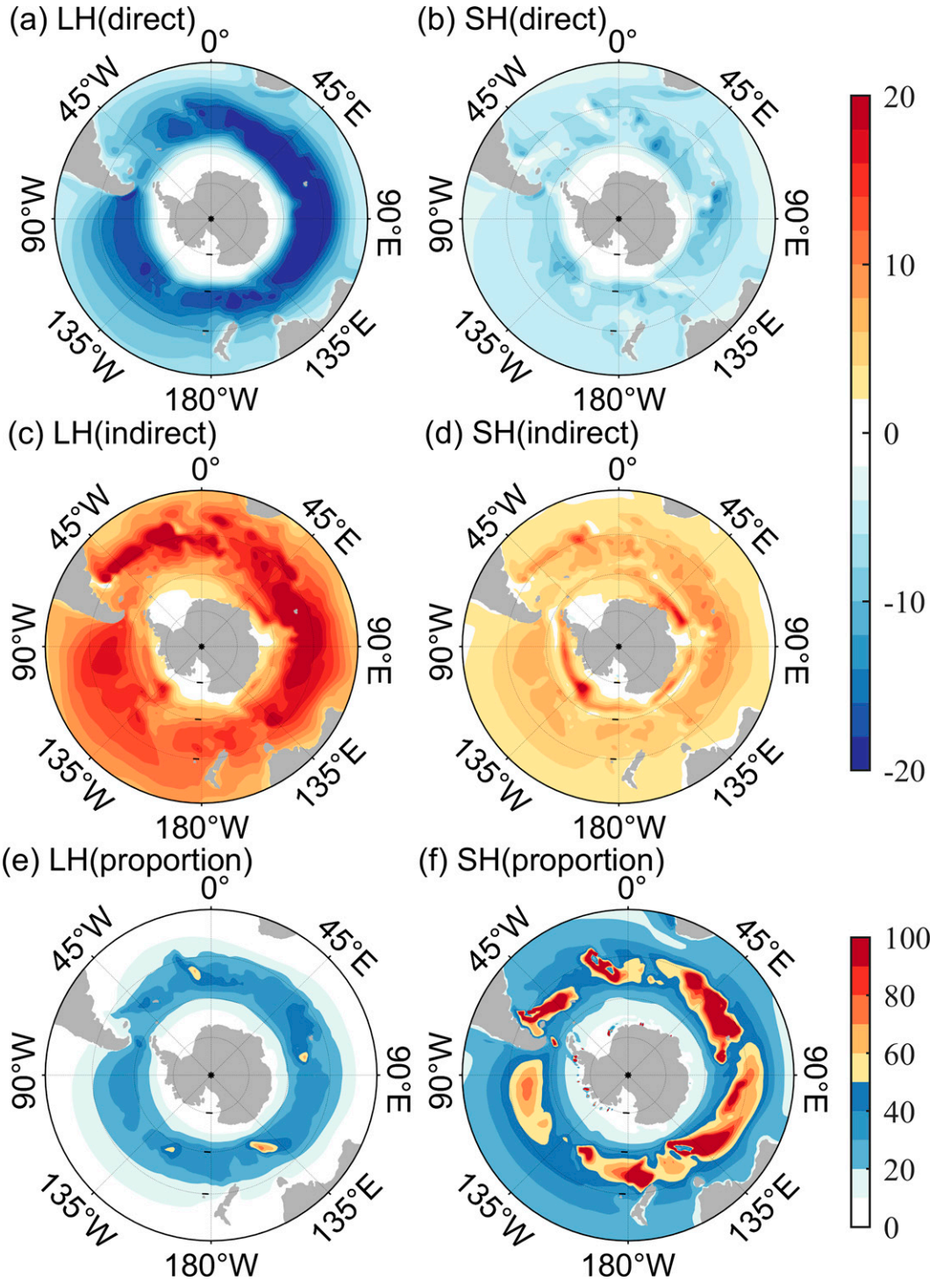

FIG. 14. Direct and indirect effects of sea spray on the latent and sensible heat fluxes (unit: W m^{-2}). The direct effect of sea spray on the heat flux is calculated based on Andreas et al. (2015), and the indirect effect on the heat flux represents the variations in the interfacial flux due to sea spray. A positive value (downward flux) indicates that the ocean absorbs heat. Shown are (a) the direct effects on the LH flux, (b) the direct effects on the SH flux, (c) the indirect effects on the LH flux, (d) the indirect effects on the SH flux, (e) the proportion of the LH variations due to sea spray (direct effects) relative to the total LH flux (unit: %), and (f) the proportion of SH variations due to sea spray (direct effects) relative to the total SH flux (unit: %).

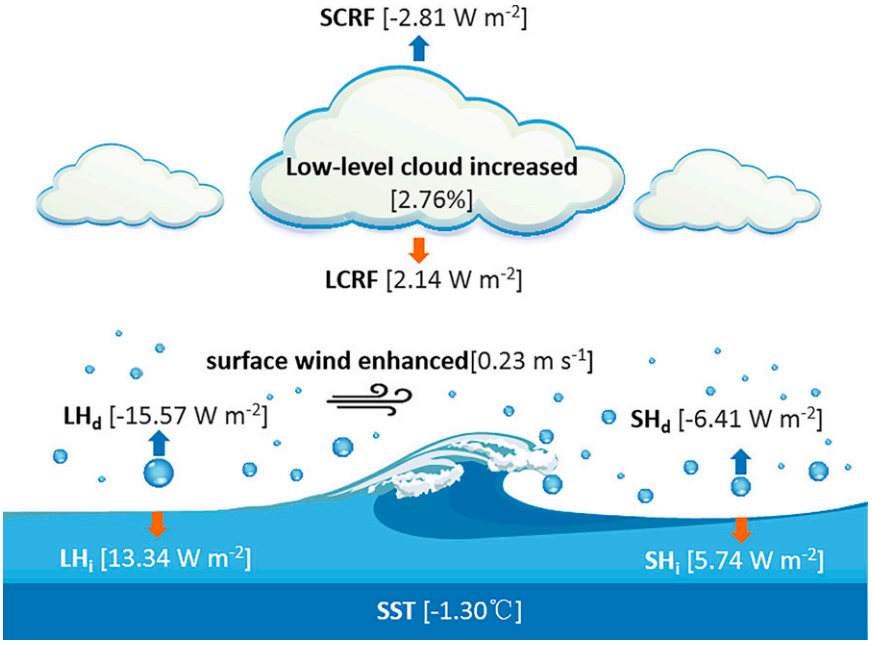

FIG. 15. Schematic diagram of the sea spray effects over the Southern Ocean (45°–60°S, 0°–360°E). LH_d (SH_d) denotes the direct effects of sea spray on the latent (sensible) heat flux. LH_i (SH_i) denotes the indirect latent (sensible) heat flux. The blue (red) arrows with negative (positive) values denote the upward (downward) flux. Enhanced heat release leads to a decreased SST and strengthened westerly winds over the Southern Ocean. The increased low-level cloud fraction results in a negative shortwave cloud radiation forcing (SCRF) and positive longwave cloud radiation forcing (LCRF) at the surface.

with the bulk spray flux algorithm was incorporated into FIO-ESM v2.0 to investigate the impacts of sea spray on heat transport at the air–sea interface and large-scale features over the Southern Ocean.

Sea spray enhanced heat and moisture exchange at the air–sea interface. The anomalous LH flux caused by sea spray accounted for more than 20%–40% of the total LH flux change, and the percentage was even higher for the SH flux. The area-averaged LH and SH fluxes due to direct sea spray effects reached −15.57 and −6.41 W m^{-2}, respectively, within the latitude band between 40° and 65°S. Furthermore, the variations in the interfacial heat flux due to sea spray, denoted as the indirect effects, exhibited the opposite direction to counteract the direct effects.

Large-scale features were affected by the sea spray effects. The LH enhancement under evaporation strengthening led to SST cooling. The area-averaged SST decreased by 1.3°C, and the zonal mean SST decreased by as much as −1.5°C near 50°S. Furthermore, this boundary condition also altered the large-scale characteristics of the atmosphere. The lower atmosphere became more stable and moister, characterized by an increase in RH at low levels. Consequently, more clouds were formed over the Southern Ocean. The liquid cloud amount, represented by the CLWP and liquid cloud content, also increased in the region from 30° to 60°S. More clouds blocked the incoming SWR and enhanced the downward LWR. The above negative cloud radiation forcing indicated that less radiation flux was received by the Southern Ocean when incorporating sea spray effects.

Consideration of the spray-mediated flux is a feasible solution to mitigate the common biases in climate models. At present, accurate simulation of climatic features over the Southern Ocean remains a long-standing challenge for climate models. The prevalent biases, characterized by warm SST and underestimated cloud cover, persist in CMIP6 models. Incorporation of the sea spray process leads to SST cooling and cloud enhancement, which provides a chance to improve model biases and achieve better simulations and predictions.

Furthermore, we attempted to estimate the direct and indirect effects of sea spray. The direct effects of sea spray were partly counteracted by the indirect effects. Positive feedback likely occurred among the sea spray–induced heat flux, SST, air temperature, and wind variations. LH and SH anomalies resulted in cooling SST and air temperature, thus changing the air pressure gradient and leading to westerly winds. In contrast, stronger winds could amplify the effects of sea spray because more droplets could be ejected from the ocean into the atmosphere combined with enhanced heat and water transport. Nevertheless, this positive feedback cannot infinitely amplify the sea spray effects, and it was found that the reduced SST, in turn, prevented evaporation over the Southern Ocean. The interfacial LH flux caused by the indirect effects of sea spray was positive, which largely counteracted

LH release due to the direct sea spray effects. In addition, Andreas (2003) proposed that the cooling air temperature could increase the air–sea temperature. In this study, the air–sea temperature decreased, leading to positive interfacial SH counteracting the SH variations due to the direct sea spray effects. Based on our results, the γ term in Eq. (2) should be negative.

This study incorporated the algorithm proposed by Andreas et al. (2015) to investigate the sea spray effects on the air–sea coupling system. We also noted that sea spray–mediated heat flux parameterizations are constantly improving. For example, Hartery et al. (2020) proposed the tuned wind speed–based parameterizations to calculate the surface flux of sea spray-generated particles. Peng and Richter (2017) investigated the contribution of different droplet sizes to sea spray–mediated fluxes. Sroka and Emanuel (2021) reviewed the available parameterizations of the enthalpy flux from sea spray. Unfortunately, there is still no consensus on which parameterization best represents the spray-mediated flux. More observations are needed to quantitatively evaluate the simulation of droplet generation, size distribution, and transport of sea spray, especially over the Southern Ocean. Moreover, the different algorithms require further verification in climate models.

Acknowledgments. All authors are thankful to the sea spray code providers, and the code can be found in Andreas et al. (2015) (http://www.nwra.com/resumes/andreas/software.php). This research was jointly supported by the National Key R&D Program of China (Grant 2018YFA0605701), the National Natural Science Foundation of China (Grants 42075039, 42022042, and 41821004), the China-Korea Cooperation Project on Northwest Pacific Marine Ecosystem Simulation under Climate Change, and the CAS Interdisciplinary Innovation Team (Grant JCTD-2020-12).

Data availability statement. The data supporting this article, including the simulation experimental data of Exp_Spray and Exp_Ctrl, are archived in the digital repository figshare (https://doi.org/10.6084/m9.figshare.19915060.v1). The CMIP6 model data used in this study can be accessed at the official website of the Earth System Grid Federation (https://esgf-node.llnl.gov), and the observational data were downloaded from the websites of the NOAA National Climatic Data Center (https://www.ncei.noaa.gov/products) and NASA CERES (https://ceres.larc.nasa.gov/data/).

APPENDIX A

Introduction of the Spinup Experiments

The spray-related experiments started from a stable initial state, which was simulated for 300 years in preindustrial state. As shown in Fig. A1, the global mean SST time series experienced a transient increase and then decreased, finally reaching a stable state in the last 50 years. The effects of sea spray reduced the global mean SST, with a 0.56°C temperature difference between Exp_Spray and Exp_Ctrl over the last 50 years. In addition, the net radiation flux at the top of the atmosphere (TOA) also reflects the energy balance state of a climate system. There initially occurred an obvious difference in the net radiation flux between these two experiments, but the difference gradually decreased with increasing integration time. The climate system reached the equilibrium state with the absorbed radiation flux matching the emitted heat flux. Furthermore, the value of the net radiation flux at the TOA in Exp_Spray was closer to zero. This indicates that the simulated Earth system became more stable by considering sea spray effects in the climate model. The 300 years interpretation before the industrial revolution provided a stable initial field for the historical simulations.

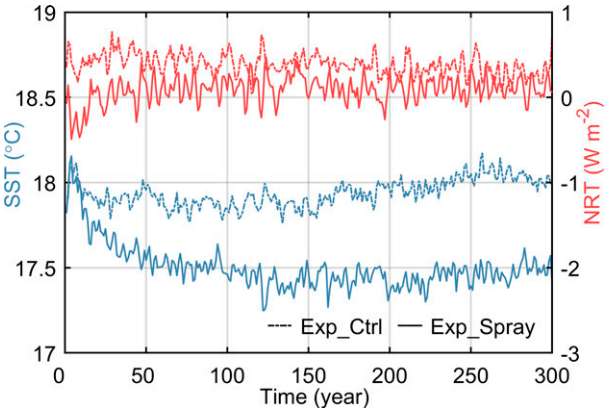

FIG. A1. Time series of the global mean SST (blue line; unit: °C) and net radiation flux at the top of the atmosphere (red line; unit: W m^{-2}) in the Exp_Spray and Exp_Ctrl experiments. The horizontal coordinate indicates the numbers of years in the preindustrial simulations.

FIO-ESM v2.0 could suitably reproduce the temporal evolution of the global warming–related SST for the period from 1850 to 2014. Figure A2a shows time series of the global mean SST retrieved from the ERSSTv5 dataset and the two experiments. The simulated SST in Exp_Ctrl was higher than that in the ERSSTv5 results. Considering the cooling effects of sea spray on SST, the temporal evolution of SST in Exp_Spray was more consistent with that based on the observations. In addition, the net radiation flux at the top of the atmosphere was analyzed (Fig. A2b). The global mean net radiation fluxes were close to zero from 1850 to 2014, indicating that the climate system is in a quasi-equilibrium state.

APPENDIX B

Introduction of the Bulk Spray–Mediated Flux Algorithm

The bulk spray–mediated flux algorithm was introduced in detail by Andreas et al. (2008, 2015), and the related calculations of variables were provided by Andreas (1992, 2003) and Andreas et al. (1995).

In Eqs. (1) and (2), ρ_w is the water density, c_{ps} is the specific heat under a constant pressure, and T_s is the 3-h SST; L_v is the LH of vaporization, expressed as a function of $T_{eq,50}$, as follows:

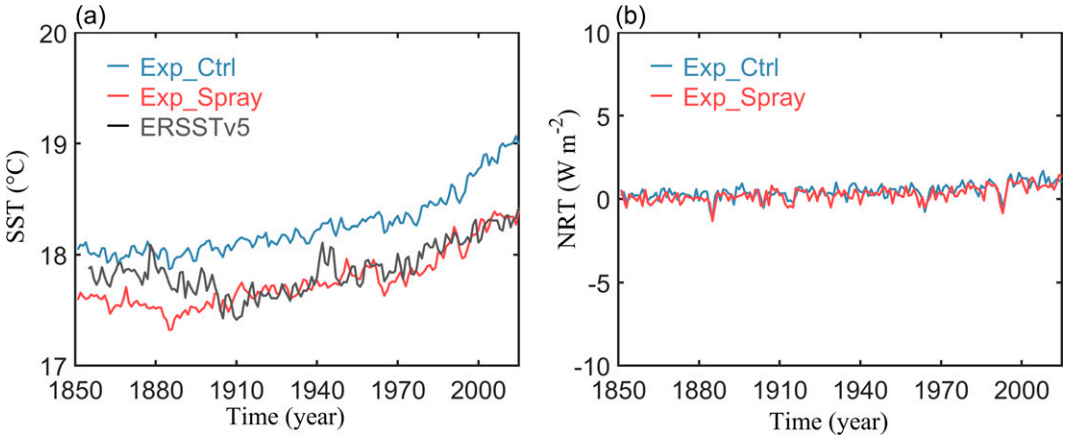

FIG. A2. Time series of (a) the global mean SST (unit: °C). The black, red, and blue lines indicate the ERSSTv5 data (1854–2014) and the simulated results in Exp_Spray and Exp_Ctrl, respectively, from 1850 to 2014. (b) Net radiation flux at the top of the atmosphere (the downward direction is positive; unit: W m^{-2}). The red and blue lines denote Exp_Spray and Exp_Ctrl results, respectively.

$$L_v = (28.34 - 0.001\,49T_{\mathrm{eq},50}) \times 10^5 \text{ for } T_{\mathrm{eq},50} < 0°\mathrm{C} \quad \text{(B1)}$$

$$L_v = (25.00 - 0.022\,74 \times T_{\mathrm{eq},50}) \times 10^5 \text{ for } T_{\mathrm{eq},50} \geq 0°\mathrm{C} \quad \text{(B2)}$$

The term T_{eq} is the temperature of 50- or 100-μm droplets in thermal equilibrium under ambient conditions before these droplets reach the equilibrium radius (Andreas 2005). Kepert (1996) devised a quick method to estimate T_{eq} via microphysical equations. Andreas (2005) slightly modified Kepert's method. Thus, T_{eq} can be calculated as follows:

$$\left\{\frac{\beta'}{T_a^2}\left[\frac{\alpha'^2}{2} - \alpha'\left(\frac{2T_a + b - 273.15}{T_a + b - 273.15}\right) + 1\right]\exp(y)\right\}\Delta T^2 + \left[1 + \frac{\beta'}{T_a}(\alpha' - 1)\exp(y)\right]\Delta T - \beta'[f - \exp(y)] = 0, \quad \text{(B3)}$$

where $a = 17.502$, $b = 240.97$, and Eq. (B3) is quadratic in ΔT, with $\Delta T = T_{\mathrm{eq}} - T_a$; also,

$$\alpha' = \frac{abT_a}{(b + T_a - 273.15)^2}, \quad \text{(B3a)}$$

$$\beta' = \frac{e_{\mathrm{sat}}(T_a)}{T_a}\frac{L_v M_w D'_w}{Rk'_a}, \quad \text{(B3b)}$$

$$y = \frac{2M_w\sigma_s}{RT_a\rho_w r} - \frac{\gamma'\varnothing_s m_s(M_w/M_s)}{(4\pi\rho_s r^3/3) - m_s}, \quad \text{(B3c)}$$

where m_s is the mass of salt in the droplet, M_s is the molecular weight of sodium chloride, M_w is the molecular weight of water, R is the universal gas constant, σ_s is the surface tension of a flat surface with the same temperature and salinity as those of droplet, γ' is the number of ions into which a sodium chloride molecule dissociates, $\varnothing_s$ is the practical osmotic coefficient, and D'_w and k'_a are values of the usual molecular diffusivity for water vapor in air (D_w) and the thermal conductivity of air (k_a), respectively, modified for the noncontinuum behavior of air and water vapor molecules around very small droplets. The terms T_a and f are the 0.5-h air potential temperature at 1000 hPa and RH at the bottom level, respectively, acquired from the atmosphere model; $e_{\mathrm{sat}}(T_a)$ is the saturation vapor pressure at temperature T_a. The 3-h SSS is acquired from the ocean model to compute constants m_s and M_s. Thus, the solution of T_{eq} involves evaluation the coefficients in Eq. (B3).

The term $r(\tau_{f,50})$ is the 50-μm droplet radius at the e-folding time scale (τ_f) parameterized as the droplet residence time in the atmosphere, and the radius r of the droplet evolves as the following function (Andreas 1992):

$$r(\tau_{f,50}) = r_{\mathrm{eq}} + (r_0 - r_{\mathrm{eq}})\exp(-\tau_f/\tau_r), \quad \text{(B4)}$$

where r_0 denotes droplets with an initial radius of 50 μm, and r_{eq} is the equilibrium radius acquired from the following recursion relation:

$$r_{k+1} = r_k - \frac{g(r_k)}{\partial g/\partial r|_{r_k}}. \quad \text{(B5)}$$

Specifically, $g(r_k)$ is a function of r, and τ_r is the e-folding times that yielding the rate of radius change, which is calculated with the following equation:

$$\tau_r = \frac{-\left.\frac{dr}{dt}\right|_{r_o} - \left[3\left(\left.\frac{dr}{dt}\right|_{r_o}\right)^2 - 2(r_0 - r_{\mathrm{eq}})^2\left.\frac{d^2r}{dt^2}\right|_{r_o}\right]^{1/2}}{\left.\frac{d^2r}{dt^2}\right|_{r_o} - \frac{1}{r_0 - r_{\mathrm{eq}}}\left(\left.\frac{dr}{dt}\right|_{r_o}\right)^2}. \quad \text{(B6)}$$

The term τ_f is the residence time in air of a spray droplet, parameterized in terms of the Hs (Andreas 1992) and the terminal falling speed $u_f(r_0)$ of a droplet with initial radius r_0 (Andreas 1992):

$$\tau_f = \frac{\mathrm{Hs}}{2u_f(r_0)}. \quad \text{(B7)}$$

Andreas and Wang (2007) developed Hs as a function of the 10-m wind speed. In this study, the 3-h Hs was provided by the MASNUM-WAM wave model.

The wind functions $V_L(u_{*,B})$ and $V_S(u_{*,B})$ were parameterized based on the combined HEXOS-FASTEX dataset (Andreas et al. 2008). Then more observations were available, and the improved wind function with two regimes can be expressed as follows:

$$V_L(u_{*,B}) = 1.76 \times 10^{-9} \text{ for } 0 \le u_{*,B} \le 0.1358 \text{ m s}^{-1}, \quad \text{(B8a)}$$

$$V_L(u_{*,B}) = 2.08 \times 10^{-7} u_{*,B}^{2.39} \text{ for } u_{*,B} \ge 0.1358 \text{ m s}^{-1}, \quad \text{(B8b)}$$

$$V_S(u_{*,B}) = 3.92 \times 10^{-8} \text{ for } 0 \le u_{*,B} \le 0.1480 \text{ m s}^{-1}, \quad \text{(B8c)}$$

$$V_S(u_{*,B}) = 5.02 \times 10^{-6} u_{*,B}^{2.54} \text{ for } u_{*,B} \ge 0.1480 \text{ m s}^{-1}. \quad \text{(B8d)}$$

Here, the friction velocity $u_{*,B}$ was updated in the coupler at 0.5-h intervals, which was also applied in the interfacial heat flux calculations.

REFERENCES

Andreas, E. L, 1992: Sea spray and the turbulent air–sea heat fluxes. *J. Geophys. Res.*, **97**, 11 429–11 441, https://doi.org/10.1029/92JC00876.

——, 2003: An algorithm to predict the turbulent air–sea fluxes in high-wind, spray conditions. Preprints, *12th Conf. on Interaction of the Sea and Atmosphere*, Long Beach, CA, Amer. Meteor. Soc., 3.4, http://ams.confex.com/ams/pdfpapers/52221.pdf.

——, 2005: Approximation formulas for the microphysical properties of saline droplets. *Atmos. Res.*, **75**, 323–345, https://doi.org/10.1016/j.atmosres.2005.02.001.

——, and J. DeCosmo, 1999: Sea spray production and influence on air–sea heat and moisture fluxes over the open ocean. *Air–Sea Exchange: Physics, Chemistry, and Dynamics*, G. L. Geernaert, Ed., Kluwer, 327–362.

——, and ——, 2002: The signature of sea spray in the HEXOS turbulent heat flux data. *Bound.-Layer Meteor.*, **103**, 303–333, https://doi.org/10.1023/A:1014564513650.

——, and S. Wang, 2007: Predicting significant wave height off the northeast coast of the United States. *Ocean Eng.*, **34**, 1328–1335, https://doi.org/10.1016/j.oceaneng.2006.08.004.

——, J. B. Edson, E. C. Monahan, M. P. Rouault, and S. D. Smith, 1995: The spray contribution to net evaporation from the sea: A review of recent progress. *Bound.-Layer Meteor.*, **72**, 3–52, https://doi.org/10.1007/BF00712389.

——, P. O. G. Persson, and J. E. Hare, 2008: A bulk turbulent air–sea flux algorithm for high-wind, spray conditions. *J. Phys. Oceanogr.*, **38**, 1581–1596, https://doi.org/10.1175/2007JPO3813.1.

——, L. Mahrt, and D. Vickers, 2015: An improved bulk air–sea surface flux algorithm, including spray-mediated transfer. *Quart. J. Roy. Meteor. Soc.*, **141**, 642–654, https://doi.org/10.1002/qj.2424.

Banzon, V., T. M. Smith, T. M. Chin, C. Liu, and W. Hankins, 2016: A long-term record of blended satellite and in situ sea-surface temperature for climate monitoring, modeling and environmental studies. *Earth Syst. Sci. Data*, **8**, 165–176, https://doi.org/10.5194/essd-8-165-2016.

Bao, Y., Z. Song, and F. Qiao, 2020: FIO-ESM version 2.0: Model description and evaluation. *J. Geophys. Res. Oceans*, **125**, https://doi.org/10.1029/2019JC016036.

Bodas-Salcedo, A., and Coauthors, 2011: COSP: Satellite simulation software for model assessment. *Bull. Amer. Meteor. Soc.*, **92**, 1023–1043, https://doi.org/10.1175/2011BAMS2856.1.

——, K. D. Williams, P. R. Field, and A. P. Lock, 2012: The surface downwelling solar radiation surplus over the Southern Ocean in the Met Office model: The role of midlatitude cyclone clouds. *J. Climate*, **25**, 7467–7486, https://doi.org/10.1175/JCLI-D-11-00702.1.

——, and Coauthors, 2014: Origins of the solar radiation biases over the Southern Ocean in CFMIP2 models. *J. Climate*, **27**, 41–56, https://doi.org/10.1175/JCLI-D-13-00169.1.

——, P. G. Hill, K. Furtado, K. D. Williams, P. R. Field, J. C. Manners, P. Hyder, and S. Kato, 2016: Large contribution of supercooled liquid clouds to the solar radiation budget of the Southern Ocean. *J. Climate*, **29**, 4213–4228, https://doi.org/10.1175/JCLI-D-15-0564.1.

Branstetter, M., 2001: Development of a parallel river transport algorithm and applications to climate studies. Ph. D. dissertation, University of Texas at Austin, 119 pp., https://repositories.lib.utexas.edu/handle/2152/10545.

Bryan, F. O., B. G. Kauffman, W. G. Large, and P. R. Gent, 1996: The NCAR CSM flux coupler. Tech. Rep. NCAR/TN-424+STR, 58 pp.

Ceppi, P., Y. Hwang, D. M. W. Frierson, and D. L. Hartmann, 2012: Southern Hemisphere jet latitude biases in CMIP5 models linked to shortwave cloud forcing. *Geophys. Res. Lett.*, **39**, L19708, https://doi.org/10.1029/2012GL053115.

Craig, A. P., M. Vertenstein, and R. Jacob, 2011: A new flexible coupler for Earth system modeling developed for CCSM4 and CESM1. *Int. J. High Perform. Comput. Appl.*, **26**, 31–42, https://doi.org/10.1177/1094342011428141.

D'Alessandro, J. J., M. Diao, C. Wu, X. Liu, J. B. Jensen, and B. B. Stephens, 2019: Cloud phase and relative humidity distributions over the Southern Ocean in austral summer based on in situ observations and CAM5 simulations. *J. Climate*, **32**, 2781–2805, https://doi.org/10.1175/JCLI-D-18-0232.1.

DeCosmo, J., K. B. Katsaros, S. D. Smith, R. J. Anderson, W. A. Oost, K. Bumke, and H. Chadwick, 1996: Air–sea exchange of water vapor and sensible heat: The Humidity Exchange over the Sea (HEXOS) results. *J. Geophys. Res.*, **101**, 12 001–12 016, https://doi.org/10.1029/95JC03796.

Dolinar, E. K., X. Dong, B. Xi, J. H. Jiang, and H. Su, 2015: Evaluation of CMIP5 simulated clouds and TOA radiation budgets using NASA satellite observations. *Climate Dyn.*, **44**, 2229–2247, https://doi.org/10.1007/s00382-014-2158-9.

Eyring, V., S. Bony, G. A. Meehl, C. A. Senior, B. Stevens, R. J. Stouffer, and K. E. Taylor, 2016: Overview of the Coupled Model Intercomparison Project Phase 6 (CMIP6) experimental design and organization. *Geosci. Model Dev.*, **9**, 1937–1958, https://doi.org/10.5194/gmd-9-1937-2016.

Fairall, C., J. D. Kepert, and G. J. Holland, 1994: The effect of sea spray on surface energy transports over the ocean. *Global Atmos. Ocean Syst.*, **2**, 121–142.

Gettelman, A., and Coauthors, 2010: Global simulations of ice nucleation and ice supersaturation with an improved cloud scheme in the Community Atmosphere Model. *J. Geophys. Res.*, **115**, D18216, https://doi.org/10.1029/2009JD013797.

Hartery, S., D. Toohey, L. Revell, K. Sellegri, P. Kuma, M. Harvey, and A. J. McDonald, 2020: Constraining the surface flux of sea spray particles from the Southern Ocean. *J. Geophys. Res. Atmos.*, **125**, e2019JD032026, https://doi.org/10.1029/2019JD032026.

Held, I. M., and Coauthors, 2019: Structure and performance of GFDL's CM4.0 climate model. *J. Adv. Model. Earth Syst.*, **11**, 3691–3727, https://doi.org/10.1029/2019MS001829.

Ho, D. T., C. S. Law, M. J. Smith, P. Schlosser, M. Harvey, and P. Hill, 2006: Measurements of air–sea gas exchange at high wind speeds in the Southern Ocean: Implications for global parameterizations. *Geophys. Res. Lett.*, **33**, L16611, https://doi.org/10.1029/2006GL026817.

Huang, B., and Coauthors, 2017: Extended Reconstructed Sea Surface Temperature, version 5 (ERSSTv5): Upgrades, validations, and intercomparisons. *J. Climate*, **30**, 8179–8205, https://doi.org/10.1175/JCLI-D-16-0836.1.

Hunke, E. C., and W. H. Lipscomb, 2008: CICE: The Los Alamos Sea Ice Model documentation and software user's manual, version 4.0, Doc. LA-CC-06-012, 76 pp.

Kay, J. E., and Coauthors, 2012: Exposing global cloud biases in the Community Atmosphere Model (CAM) using satellite observations and their corresponding instrument simulators. *J. Climate*, **25**, 5190–5207, https://doi.org/10.1175/JCLI-D-11-00469.1.

——, C. Wall, V. Yettella, B. Medeiros, C. Hannay, P. Caldwell, and C. Bitz, 2016: Global climate impacts of fixing the Southern Ocean shortwave radiation bias in the Community Earth System Model (CESM). *J. Climate*, **29**, 4617–4636, https://doi.org/10.1175/JCLI-D-15-0358.1.

Kepert, J. D., 1996: Comments on "The temperature of evaporating sea spray droplets." *J. Atmos. Sci.*, **53**, 1634–1641, https://doi.org/10.1175/1520-0469(1996)053<1634:COTOES>2.0.CO;2.

Kuma, P., and Coauthors, 2020: Evaluation of Southern Ocean cloud in the HadGEM3 general circulation model and MERRA-2 reanalysis using ship-based observations. *Atmos. Chem. Phys.*, **20**, 6607–6630, https://doi.org/10.5194/acp-20-6607-2020.

Lasher-Trapp, S., E. L. Scott, E. Järvinen, M. Schnaiter, F. Waitz, P. J. DeMott, C. S. McCluskey, and C. J. H. Thomas, 2021: Observations and modeling of rime splintering in Southern Ocean cumuli. *J. Geophys. Res. Atmos.*, **126**, e2021JD035479, https://doi.org/10.1029/2021JD035479.

Lawrence, D. M., and Coauthors, 2011: Parameterization improvements and functional and structural advances in version 4 of the Community Land Model. *J. Adv. Model. Earth Syst.*, **3**, M03001, https://doi.org/10.1029/2011MS000045.

Li, J. F., D. E. Waliser, G. Stephens, S. Lee, T. L'Ecuyer, S. Kato, N. Loeb, and H. Ma, 2013: Characterizing and understanding radiation budget biases in CMIP3/CMIP5 GCMs, contemporary GCM, and reanalysis. *J. Geophys. Res. Atmos.*, **118**, 8166–8184, https://doi.org/10.1002/jgrd.50378.

Ling, S. C., and T. W. Kao, 1976: Parameterization of the moisture and heat transfer process over the ocean under the whitecap sea states. *J. Phys. Oceanogr.*, **6**, 306–315, https://doi.org/10.1175/1520-0485(1976)006<0306:POTMAH>2.0.CO;2.

Liu, J., J. A. Curry, C. A. Clayson, and M. A. Bourassa, 2011: High-resolution satellite surface latent heat fluxes in North Atlantic hurricanes. *Mon. Wea. Rev.*, **139**, 2735–2747, https://doi.org/10.1175/2011MWR3548.1.

Mason, S., J. K. Fletcher, J. M. Haynes, C. Franklin, A. Protat, and C. Jakob, 2015: A hybrid cloud regime methodology used to evaluate Southern Ocean cloud and shortwave radiation errors in ACCESS. *J. Climate*, **28**, 6001–6018, https://doi.org/10.1175/JCLI-D-14-00846.1.

Neale, R. B., and Coauthors, 2010: Description of the NCAR Community Atmosphere Model (CAM5.0). NCAR Tech. Note NCAR/TN-486+STR, 289 pp.

Peng, T., and D. Richter, 2017: Influence of evaporating droplets in the turbulent marine atmospheric boundary layer. *Bound. Layer Meteor.*, **165**, 497–518, https://doi.org/10.1007/s10546-017-0285-7.

——, and ——, 2019: Sea spray and its feedback effects: Assessing bulk algorithms of air–sea heat fluxes via direct numerical simulations. *J. Phys. Oceanogr.*, **49**, 1403–1421, https://doi.org/10.1175/JPO-D-18-0193.1.

Persson, P. O., J. E. Hare, C. W. Fairall, and W. D. Otto, 2005: Air–sea interaction processes in warm and cold sectors of extratropical cyclonic storms observed during FASTEX. *Quart. J. Roy. Meteor. Soc.*, **131**, 877–912, https://doi.org/10.1256/qj.03.181.

Petersen, G. N., and I. A. Renfrew, 2009: Aircraft-based observations of air–sea fluxes over Denmark Strait and the Irminger Sea during high wind speed conditions. *Quart. J. Roy. Meteor. Soc.*, **135**, 2030–2045, https://doi.org/10.1002/qj.355.

Platnick, S., M. D. King, S. A. Ackerman, W. P. Menzel, B. A. Baum, J. C. Riedi, and R. A. Frey, 2003: The MODIS cloud products: Algorithms and examples from Terra. *IEEE Trans. Geosci. Remote Sens.*, **41**, 459–473, https://doi.org/10.1109/TGRS.2002.808301.

Qiao, F., Y. Yuan, Y. Yang, Q. Zheng, C. Xia, and J. Ma, 2004: Wave-induced mixing in the upper ocean: Distribution and application to a global ocean circulation model. *Geophys. Res. Lett.*, **31**, 293–317, https://doi.org/10.1029/2004GL019824.

——, Z. Song, Y. Bao, Y. Song, Q. Shu, C. Huang, and W. Zhao, 2013: Development and evaluation of an Earth system model with surface gravity waves. *J. Geophys. Res. Oceans*, **118**, 4514–4524, https://doi.org/10.1002/jgrc.20327.

——, and Coauthors, 2016: A highly effective global surface wave numerical simulation with ultra-high resolution. *Proc. Int. Conf. for High Performance Computing, Networking, Storage and Analysis (SC'16)*. Salt Lake City, UT, IEEE, https://doi.org/10.1109/SC.2016.4.

Richter, D. H., and D. P. Stern, 2014: Evidence of spray-mediated air–sea enthalpy flux within tropical cyclones. *Geophys. Res. Lett.*, **41**, 2997–3003, https://doi.org/10.1002/2014GL059746.

——, and F. Veron, 2016: Ocean spray: An outsized influence on weather and climate. *Phys. Today*, **69**, 34–39, https://doi.org/10.1063/PT.3.3363.

Smith, R., and Coauthors, 2010: The Parallel Ocean Program (POP) reference manual: Ocean component of the Community Climate System Model (CCSM). Rep. LAUR-01853, 141 pp., http://n2t.net/ark:/85065/d70g3j4h.

Soden, B. J., and G. A. Vecchi, 2011: The vertical distribution of cloud feedback in coupled ocean–atmosphere models. *Geophys. Res. Lett.*, **38**, L12704, https://doi.org/10.1029/2011GL047632.

Song, Z., F. Qiao, X. Lei, and C. Wang, 2012: Influence of parallel computational uncertainty on simulations of the coupled general climate model. *Geosci. Model Dev.*, **5**, 313–319, https://doi.org/10.5194/gmd-5-313-2012.

——, Y. Bao, D. Zhang, Q. Shu, Y. Song, and F. Qiao, 2020: Centuries of monthly and 3-hourly global ocean wave data for past, present, and future climate research. *Sci. Data*, **7**, 226, https://doi.org/10.1038/s41597-020-0566-8.

Sroka, S., and K. Emanuel, 2021: A review of parameterizations for enthalpy and momentum fluxes from sea spray in tropical cyclones. *J. Phys. Oceanogr.*, **51**, 3053–3069, https://doi.org/10.1175/JPO-D-21-0023.1.

Trenberth, K. E., and J. T. Fasullo, 2010: Simulation of present-day and twenty-first-century energy budgets of the Southern Oceans. *J. Climate*, **23**, 440–454, https://doi.org/10.1175/2009JCLI3152.1.

Vignesh, P. P., J. H. Jiang, P. Kishore, H. Su, T. Smay, N. Brighton, and I. Velicogna, 2020: Assessment of CMIP6 cloud fraction and comparison with satellite observations. *Earth Space Sci.*, **7**, e2019EA000975, https://doi.org/10.1029/2019EA000975.

Wang, C., L. Zhang, S. Lee, L. Wu, and C. R. Mechoso, 2014: A global perspective on CMIP5 climate model biases. *Nat. Climate Change*, **4**, 201–205, https://doi.org/10.1038/nclimate2118.

Zhao, B., F. Qiao, L. Cavaleri, G. Wang, L. Bertotti, and L. Liu, 2017: Sensitivity of typhoon modeling to surface waves and rainfall. *J. Geophys. Res. Oceans*, **122**, 1702–1723, https://doi.org/10.1002/2016JC012262.